Biological Systems Engineering--Dissertations, Theses, and Student Research

Biological Systems Engineering

Fall 12-2021

High-Frequency Unmanned Aircraft Flights For Crop Canopy Imaging During Diurnal Moisture Stress

Suresh Pradhyun Kashyap

University of Nebraska - Lincoln, skashyap3@huskers.unl.edu

HIGH-FREQUENCY UNMANNED AIRCRAFT

FLIGHTS FOR CROP CANOPY IMAGING DURING

DIURNAL MOISTURE STRESS

by

Suresh Pradhyun Kashyap

A THESIS

Presented to the Faculty of

The Graduate College at the University of Nebraska

In Partial Fulfillment of Requirements

For the Degree of Master of Science

Major: Agricultural and Biological Systems Engineering

Under the Supervision of Professors Derek M. Heeren and
Wayne E. Woldt

Lincoln, Nebraska

December, 2021

HIGH-FREQUENCY UNMANNED AIRCRAFT FLIGHTS FOR CROP CANOPY IMAGING DURING DIURNAL MOISTURE STRESS

Suresh Pradhyun Kashyap, M.S.

University of Nebraska, 2021

Advisors: Derek M. Heeren and Wayne E. Woldt

Previous research has used unmanned aerial vehicle (UAV) technology for calculating CWSI (Crop Water Stress Index) values in the context of irrigation scheduling. Typically, these estimations were taken at one time of day, usually near or shortly after solar noon. A significant limitation with these CWSI values is that the UAV thermal imagery captured at this point in time can be affected by various factors like atmospheric air temperature, sun radiation, wind speed, relative humidity, and other micrometeorological disturbances in the air. In order to address these temporal effects, high-frequency UAV flights were conducted over different daylight hours to analyze and compare the CWSI values to create a better understanding of the crop dynamics to irrigation events. In addition, another stress index which requires fewer input data, the Degrees Above Non-Stressed (DANS), were also compared to CWSI values. This research was carried out at three different field research sites in Nebraska: Two at the Eastern Nebraska Research and Extension Center (ENREC), Mead, NE and one at the Irmak Research Laboratory (IRK) in South Central Agricultural Laboratory (SCAL), Clay Center, NE. All fields were growing soybean with various levels of irrigation and rainfed treatments. A DJI M600 UAV was used with MicaSense RedEdge multispectral

camera and a FLIR Duo Pro R thermal camera to capture imagery, flying at an altitude of 400 m above ground level. In addition, local meteorological data and ground-based IRT (Infrared Thermometer) data were collected. In order to calculate CWSI and DANS, a thermal calibrated linear regression model developed by NU-AIRE Lab, UNL, NE, was also used to improve the accuracy of the thermal imagery data. NDVI and NDRE values were also computed to find any correlation between affecting CWSI values. Both thermal and multispectral imagery is used to analyze the spatiotemporal dynamics of the crop.

ACKNOWLEDGEMENTS

It is my pleasure to acknowledge all those who have contributed to the work described in this thesis. My first and foremost thanks go to my primary academic advisor, Dr. Derek M. Heeren, for accepting me in his research group. Throughout my graduate school experience, he gave me intellectual freedom in my work, supported my attendance at various conferences, exposed me to new ideas, and demanded high standards of work from me. Second, I would like to thank my co-advisor, who was also my primary advisor during the start of my master's program, Dr. Wayne E. Woldt, to take me as his last student before being an emeritus professor, who made this thesis study possible. His friendly guidance and expert advice were invaluable throughout all phases of the project. In addition, I would like to thank my committee members Dr. Suat Irmak, Dr. Yeyin Shi, and Dr. Christopher Neale for their interest, support and expertise in providing me invaluable help for this thesis, and for their comments and suggestions during my defense.

Throughout this thesis, every result was accomplished with the help and support of my fellow project members and collaborators Dr. Mitchell Maguire, Dr. Jasreman Singh, and Mr. Sandeep Bhatti. I would also like to thank all my Professors for my completion of course work and projects by keeping me motivated during the my time of study. I would also like to extend my gratitude to Mr. Alan Boldt, Mr. Eric Wilkening, Mr. Matthew Druidik for providing me help in the selected research fields for this thesis.

In addition, I would like to thank Robert B. Daugherty Water for Food Global Institute at the University of Nebraska in funding my master's study through Graduate

Research Assistantship and acknowledge the Department of Biological Systems Engineering of University of Nebraska – Lincoln. I would like to thank Dr. David Jones for always being supportive and helping me in my needs. Many thanks to Mrs. Christel Burgason and Mr. Sang Ho for their help in regarding any departmental needs.

Finally, I would like to acknowledge my family who supported me during my time here. I would like to thank my Mom, Dad, Sister, Grand Parents, Uncle and Aunts for being my backbone throughout my journey. I would also like to thank my friends and roommates for their support and remarkable memories especially Mr. Sai Chand, Mr. Guru Charan, Mr. Puranjith and Mr. Gautam Takoo, Mr. Ranjith Kumar. I apologize in advance if I missed mentioning the names of those who helped with my research and friends. My sincere gratitude goes out to everyone I met in this university for always encouraging me in my pursuits and inspiring me to pursue my dreams.

TABLE OF CONTENTS

LIST OF TABLES

LIST OF FIGURES

CHAPTER 1. INTRODUCTION

1.1 Irrigation in Nebraska

Irrigation plays a crucial role in improving agricultural productivity in today's world. According to Payero (Irmak, 2006), irrigated agriculture in Nebraska generates approximately $5 billion in income every year, with corn and soybeans being the most important cultivated crops. Primary irrigation for these crops is being provided by pumping groundwater from the High Plain Aquifer, which is a water storage basin beneath ten neighboring states. The most common source of irrigation water was groundwater and precipitation. Over time, it has been revealed that these water sources are depleting, resulting in widespread water shortages. As a consequence, farmers have been pushed to evaluate and adopt efficient irrigation systems, with the many agronomists and researchers focusing on irrigation efficiency.

The history of changes and applications of irrigation methods transformed radically in Nebraska. In the early 1940s, surface irrigation was carried out by furrows, borders, or flooding from ditches, also known as gravity irrigation. Later, after World War II, with the introduction of pressurized and moving irrigation systems, Frank Zyback from Colorado, in 1948, invented a center-pivot sprinkler irrigation system to reduce human resources needs and solve problems with seepage and deep percolation losses of the gravity-flow irrigation systems. With this invention and based on studies conducted by the University of Nebraska Remote Sensing Center (UNL, 1977), the installation of pivots had rapidly increased from 2700 units in 1972 to 12,000 units in 1976. In just a few years, that number increased by 6% to 78% (USDA-NASS, 2008), and by 2018, 91%

(USDA-NASS, 2019a) of the irrigated acres in Nebraska were irrigated exclusively using center pivot technology (Evett et al., 2020).

With the increasing demand for Center Pivot Irrigation (CPI) systems and an urge to improve its efficiency and performance, terms like Precision Irrigation (PI) Technologies and Variable Rate Irrigation (VRI) technologies came into existence. Using these new technologies, irrigation management practices can be improved spatially, and over-irrigation can be reduced. Several researchers have been working on these technologies to improve crop and soybean production (Neale et al., 2012; Evans et al., 2013; Stone et al., 2015; O'Shaughnessy et al., 2016, 2019; Sui and Yan, 2017; Woldt et al., 2018; Barker et al., 2018, 2019; Bhatti et al., 2018; Maguire, 2018; 2021; Singh et al., 2021).

1.2 Effects of Climate Change on Irrigation Scheduling

In the previous discussion, rapid changes in irrigation methods have been discussed. In the coming decades, climate change is expected to have significant impacts on agricultural production. In order to effectively manage water resources, watershed managers and agricultural producers need to understand the impacts of climate change on irrigation demand for crop production in their region. From the recent studies, Tebaldi et al., (2006), stated that these climate changes would vary by latitude, particularly in the U.S. central Great Plains, causing air temperatures to be increased and precipitation levels to be decreased. The duration of heatwaves can also be expected to increase by 5-10 days during the growing season (Evatt et al., 2020).

In general, irrigation scheduling is majorly determined based on meteorological parameters. In order to achieve maximum productivity, crops require favorable climate conditions. These effects can be explained in terms of crop water stress, that is, loss of moisture due to transpiration. Due to this moisture loss and insufficient cooling mechanism, canopy temperature increases. In calm and humid conditions, all plants transpire slowly, and the canopy temperature is close to the air temperature no matter how severe the water stress; similarly, sweat evaporates slowly and does not contribute significantly to cooling under these conditions. During windy and dry conditions, non-stressed plants transpire rapidly and are cooler than the air temperature, whereas stressed crops transpire slowly and are warmer than the air temperature. Concerning the duration of the day and weather conditions, canopy temperature may rise or be reduced (Lo et al., 2018).

On the other hand, variability in precipitation could also accelerate water stress conditions and the frequency of extreme events, resulting in negative consequences for crop yields (Porter and Semenov, 2005; Nandan et al., 2021). Many farmers and agronomists predict precipitation based on historical weather data classifying it into a dry or wet year. However, due to the impacts of climate change, this information is unpredictable.

Considering these issues, many researchers regularly monitor evapotranspiration and water stress in crops to optimize irrigation management and maximize water efficiency to mitgate the negative impacts of climate change.

1.3 Evapotranspiration for Irrigation Management

General definition of evapotranspiration (ET) can be defined as the loss of water from the soil to the atmosphere by both, evaporation of water and transpiration from plants. To understand the complex process of water loss in crops and to assess agricultural water requirement, estimation of evapotranspiration is becoming essential for optimal irrigation planning. In understanding ET, comprehensive knowledge on land surface fluxes, particularly their latent and sensible components, will also be essential. There are several methods traditionally used to measure evapotranspiration (ET) at the field scale (Bowen ratio, eddy correlation system, soil water balance), but these methods are not effective in estimating fluxes on large spatial scales (Courault et al., 2005).

For operational purposes, water managers and irrigation engineers require accurate estimates of surface fluxes, specifically ET. Many countries use the FAO 56 method today. The method involves estimating crop evapotranspiration (ET_c) with a reference evapotranspiration (ET_r) and a crop coefficient (K_c), where ET_r is retrieved using the Penman–Monteith method (Allen et al., 1998, FAO 56 method).

Nevertheless, surface resistance to vapor transport can vary depending on the time of the day, weather conditions, especially available radiation and vapor pressure deficit (Ortega et al., 2004). Moreover, the determination of crop coefficients is also in dispute since many factors are involved (Neale et al., 2005). In non-standard conditions, the ET crop surfaces are either adjusted by a water stress coefficient or by modifying the K_c coefficient. According to weather conditions, crop factors, management and environmental conditions, actual evapotranspiration (ET_a) corresponds to the actual water

consumption. However, several other characteristics of the crop and the surface have to be considered: crop type, variety and stage of development, ground cover, and root system development (Courault et al., 2005)

By applying remote sensing data with an increasing spatial and temporal resolution, such information can be provided on a variety of timescales and spatial scales. Numerous methods have been developed for estimating surface fluxes using this information. Classifying these methods is always challenging since their complexity depends on the balance between empirical and physical components.

1.4 Remote Sensing based estimation of Evapotranspiration

Various researchers have proposed methods to estimate evapotranspiration based on remote sensing. Field-based ET methods are commonly categorized into weather-based methods, surface energy balance methods (SEBM), and soil moisture measurements (Allenet al., 1998; Allen, 2000; Zhao-Lianget al., 2009). The estimation of ET using remote sensing (RS) has been used with various sensors. The image data from satellites has been a major input for ET estimation for the past 17 years (Xia et al., 2016). For estimates of ET at regional scales, the RS approach is known as one of the most reliable and efficient methods (Kustas and Anderson, 2009) (Park et al., 2018).

In general, four types of RS methods for estimating ET have been proposed: 1) empirical direct method; 2) residual method; 3) inference method, in which a potential (or reference) ET is calculated from ground measurements and RS data are used to estimate crop coefficients; and 4) deterministic method based on the Soil-Vegetation-Atmospheric Transfer (SVAT) model (Courault et al., 2005; Calcagno et al., 2007; Nouri et al., 2015,

Park et al 2018). The most common menthod that relies on estimating ET is the

difference between surface and air temperature (Jackson et al., 1977; Seguin and Itier,

1983, Park et al., 2018), equation:

$$ET_{\text{daily}} = R_{n,\text{daily}} + A - B\left(T_{s,\text{midday}} - T_{a,\text{midday}}\right) \tag{1}$$

where A and B are coiefficients, ET_{daily} is the daily ET; $R_{n,daily}$ is the daily net

radiation; $T_{s,midday}$ is the surface temperature measured at midday, and $T_{a,midday}$ is the air

temperature measured at midday.

The residual method, which makes use of the surface energy balance model

(SEBM), has been widely used to estimate ET, with ET being obtained as a residual

(latent heat flux, LE, or ET) in SEBM and the other energy balance components (net

radiation, sensible heat flux, and soil heat flux) being estimated using a combination of

empirical and physical relationships (Su, 2002; Kalma et al., 2008):

$$\lambda ET = R_n - H - G \tag{2}$$

where λET is the latent heat flux (W/m2), Rn is the net radiation at the surface

(W/m2), H is the sensible heat flux to the air (W/m2) and; G is the soil heat flux (W/m2)

According to the researchers Chávez and Neale et al. (2008), the instantaneous

latent heat flux is a tool that can be used to determine and estimate the rate of

evapotranspiration of crops (ET_d) daily. The input for the latent heat flux can be retrieved

from RS imagery, which is multispectral and digitally airborne. In the quantitative

research study, the researchers conducted the study and collected data from a 12 km by

22 km area field for corn and soybean crops located in Ames, Iowa. The researchers

applied six methods to estimate the errors, with the observations being that the range of

the errors varied from -5.7 ± 4.8% (MBE ± RMSE) to 26.0 ± 15.8%. Based on this

research, the values extrapolated ET_d in reference with the evaporative fraction (EF) give

better results when compared with ET values of eddy covariance. With an average

estimation error of about-0.3mm per day, the ET_d variance in prediction provides an

average of about 5.7 ± 4.8% in comparison to the values from the eddy covariance energy

balance systems. Other methods used in this research study are the solar radiation-based

ET_a extrapolation method and the alfalfa reference method based on ET extrapolation.

Both perform relatively well for both crops investigated in the research case experiment.

Therefore, the research emphasizes that the daily heat flux should be included in the ETd

especially when the EF method is used. Hence, researchers validated the use of the

methodology of the RS-based ET, which uses airborne multispectral concepts.

Bhatti et al., (2018) narrowed his focus on the Variable Rate Irrigation (VRI),

where the studies address that the characteristics of the plants have a spatial variance with

the field characteristics. In the management of agricultural fields, applying the depth of

irrigation uniformly in the area helps reduce water losses, as supported by VRI. Hence,

the research aims to use the spatial evapotranspiration (*ET*) model to quantify the VRI

potential and how it impacts the crop-water response compared to the other models such

as infrared and uniform treatments. The research makes use of four main treatments,

namely; 1) infrared treatment, 2) Landsat imagery using VRI, 3) uniform treatment, and

4) use of VRI unnamed aerial imagery system (UAS).

1.5 Monitoring Crop Water Stress for Irrigation Management

In order to schedule irrigation effectively, crop water stress status must be

monitored. Timely detection of water stress in agricultural fields is difficult since symptoms typically appear visually when crops are already highly water-stressed. To ensure that crops remain productive on a sustainable basis, the monitoring of water stress in crops as early as possible is critical. Previous studies established a variety of indicators for predicting agricultural water stress based upon measurements of the energy balance between soil, plants, and the atmosphere. A decrease in transpiration rate causes a rise in leaf temperature when plants are experiencing a water shortage. As a result, their stomata close partly. In response to this phenomena, Idso et al. (1981) and Jackson et al. (1981) developed an empirical and therotical crop water stress index (CWSI). The empirical method relies on the relationship between canopy-to-air temperature difference and vapor pressure deficit (VPD). Whereas, the theoretical method applies surface energy balance equation to account for variations in climate, and calculates the distance between the upper and lower boundaries of canopy-to-air temperature difference (Han et al., 2018). The equation of CWSI (Idso et al., 1981) can represented as:

$$CWSI = \frac{(T_c - T_a) - (T_{\text{lower}} - T_a)}{(T_{\text{upper}} - T_a) - (T_{\text{lower}} - T_a)} \tag{3}$$

where, T_{lower} is represenetd as the lower baseline temperature of a non-water-stressed canopy; and T_{upper} is represenetd as the upper baseline temperature of a water stressed canopy

Jackson et al. (1981), in his same paper, also proposed CWSI based on evapotranspiration, in which leaf transpiration cools the canopy surface in non-water stressed plants. That is, through periods of water stress, leaf transpiration drops and the

canopy temperature rises in water-stressed plants due to a lack of water in the root zone. Therefore, CWSI can also be calculated as a ratio between actual evapotranspiration (ETa) and potential evapotranspiration (ETp) of plant, equation (2):

$$CWSI = 1 - \frac{ETa}{ETp} \tag{4}$$

Later, Jones et al., (1992), reformulated the calculation CWSI based on using wet and reference temperatures in the field,. The approach has signifacntly reduced the use of various measuremts of meterological data (required for upper and lower basline calculations). The equation is as follows:

$$CWSI = \frac{T_c - T_{wet}}{T_{dry} - T_{wet}} \tag{5}$$

where, T_c represents canopy temperature; T_{wet} represents to the reference temperature at full transpirating leaf; and T_{dry} represents to the referenc temperature of non-transpiring leaf.

CWSI relies on manual or continuous point measurements to measure canopy temperature (T_c) of the desired crop. Many researcher continue to use, multiple infrared thermometers (IRTs) in the field for monitoring the crop stress (Irmak et al., 2000; Payero and Irmak, 2006; Peters and Evett, 2008; O ' Shaughnessy et al., 2017, 2012; Taghvaeian et al., 2012; Candogan et al., 2013; DeJonge et al., 2015; Singh et al., 2021; Maguire et al., 2021).

In recent years, various remote sensing (RS) platforms have become widely accessible, enabling several studies to be conducted using unmanned aerial vehicles (UAVs) equipped with sensors as a major input, aiming to replace ground-based measurements, and

to make them applicable to larger or field production scale (Woldt et al., 2018). For agricultural studies, a range of customizable sensors is also available for all types of UAS platforms. For measuring specific spectral information, high resolution digital cameras, multispectral cameras, and hyperspectral imaging systems, and thermal cameras are being used (Shafian and Shi et al., 2018). Hence, with the advancements of UAV technology and thermal sensor, several studies have been conducted on crop water stress for extracting T_c. This appreaoch have also led to further simplify the calculation of CWSI by reducing or eliminating the use of ground-based measurements or IRTs, to make it applicable at field scale.

Recently, a statistical approach of calculating CWSI, was used, based on histogram analysis of canopy temperature (Meron et al., 2010 & Rud et al., 2014) that included in the delineation of canopy pixels and calculating T_{wet} from the lowest 5% of temperature histogram and T_{dry} to be equal to the air temperature (T_{air}) + 5 ∘C (Irmak, 2002). Park et al., (2017) redeveloped the above statistical CWSI approach that can be adaptable to variability over the whole field by stating, that having a single set of T_{wet} and T_{dry} values will result in inaccurate estimations of CWSI. He considered employing thersholding of T_{wet} and T_{dry} for each sub-regions by extracting from the critical values of 99% confidence intervals of canopy temperature distribution. This new approach, does not require any meteorological data and reference surfaces, thereby reducing the complexity of estimating the CWSI spatially.

1.6 Remote Sensing based estimation of Crop Water Stress

Methods based on canopy temperature have been recognized as a sensitive technique for detecting plant water stress (Cohen et al., 2005). Water stress has an influence on the stomatal conductance (SC) and transpiration of leaves, resulting in a rise in canopy

temperature. Rather of directly measuring stomatal conductance using leaf gas exchange methods, infrared thermometry (IRT) approaches for detecting stomatal closure and estimating conductance have been developed (Jones, 1999; Jones et al., 2002; Leinonen et al., 2006; Fuentes et al., 2012). Direct measurements may be cumbersome when a significant volume of leaves is required for sample (Jones, 1999). The IRT notion is based on the fact that leaf temperature tends to rise as stomata close, since this reduces transpiration and hence the cooling impact of leaves. Jones (1999) presented an index (Ig) that has a direct linear connection with stomatal conductance based on this approach.

The Photochemical Reflectance Index (PRI) has been used to anticipate agricultural water stress by providing an index of changes in photosynthetic pigments in leaves. PRI had a strong connection with plant-based indicators of water stress (leaf water potential and stomatal conductance) in a case study conducted in a citrus orchard (Zarco-Tejada et al., 2012). Berni et al. (2009b) proposed an improved PRI, dubbed the Normalised Photochemical Reflectance Index (PRInorm), which utilizes a new PRI normalized by the Renormalized Difference Vegetation Index (RDVI) and a red edge index. PRInorm demonstrated a stronger association with a plant-based water stress indicator because to its sensitivity in detecting changes in the xanthophyll pigment and decreased leaf area induced by water stress (Gago et al., 2015).

Other vegetation indicators have been investigated for their potential to identify plant water stress. In comparison to the NDVI, the Optimized Soil Adjusted Vegetation Index (OSAVI) and the Transformed Chlorophyll Absorption in Reflectance Index (TCARI) are canopy structural indices that have shown superior performance by limiting the

influence of soil reflectance (Haboudane et al., 2002; Zarco-Tejada et al., 2012). Haboudane et al. (2002) proposed a ratio (TCARI/OSAVI) specifically for the purpose of properly forecasting chlorophyll concentration. Additionally, it has been shown that the ratio is sensitive to changes in the canopy structure cover caused by plant water stress (Zarco-Tejada et al., 2012; Gago et al., 2015).

Using just TIR imaging, a histogram-based technique has been developed to differentiate the canopy temperature from the soil temperature (Meron et al., 2003; Meron et al., 2010a). The approach makes use of the TIR image's pixel histogram and a constant threshold (e.g., the coldest 33% of the histogram) to extract canopy-related temperatures from the histogram. The threshold indicates the histogram's border for vegetation and soil distribution, and its value is established using statistical and empirical approaches. The research demonstrated that the process of CWSI calculation might be expedited and simplified by obviating the necessity for VIS image processing.

Park et al., 2021 in his research, used unmanned aerial vehicle (UAV) to form the basis of the study. The method monitors the status of the crop water on a real-time basis. This facilitates timely and efficient irrigation scheduling by enabling an accurate strategy for decision-making. The approach used in this research is based on an analysis of the UAV input collected for water stress and presented against other physiological parameters of the crops. Based on the finding of the quantitative and qualitative analysis of the data, the researchers concluded that efficacy and consistency of water values were higher when the data was collected during the period between mid-morning and midafternoon.

1.7 References

Allen, R. G. (2000) Using the FAO-56 dual crop coefficient method over an irrigated region as part of an evapotranspiration intercomparison study. Journal of Hydrology, 229, 27-41.

Allen, R. G., Pereira, L. S., Raes, D., Smith, M. and others (1998) Crop Evapotranspiration: Guidelines for computing crop water requirements. F. A. O. Irrig. Drain. Pap., 300, D05109.

Barker, J.B., Bhatti, S., Heeren, D.M., Neale, C.M.U., Rudnick, D.R., 2019. Variable rate irrigation of maize and soybean in West-Central Nebraska under full and deficit ir-rigation. Front. Big Data 2 (34).https://doi.org/10.3389/fdata.2019.00034.

Barker, J.B., Heeren, D.M., Neale, C.M.U., Rudnick, D.R., 2018b. Evaluation of variable rate irrigation using a remote-sensing-based model. Agric. Water Manage. 203, 63–74.https://doi.org/10.1016/j.agwat.2018.02.022.

Bhatti, S. (2018). Variable Rate Irrigation Using a Spatial Evapotranspiration Model With Remote Sensing Imagery and Soil Water Content Measurements.

Bhatti, S., 2018. Variable Rate Irrigation Using a Spatial Evapotranspiration Model With Remote Sensing Imagery and Soil Water Content Measurements. M.S. Thesis. Department of Biological Systems Engineering, University of Nebraska, Lincoln, Nebraska.

Bian, J., Zhang, Z., Chen, J., Chen, H., Cui, C., Li, X., ... & Fu, Q. (2019). Simplified
   evaluation of cotton water stress using high resolution unmanned aerial vehicle
   thermal imagery. Remote Sensing, 11(3), 267.

Chávez, J. L., Neale, C. M., Prueger, J. H., & Kustas, W. P. (2008). Daily
   evapotranspiration estimates from extrapolating instantaneous airborne remote
   sensing ET values. Irrigation Science, 27(1), 67-81.

Chávez, J. L., Neale, C. M., Prueger, J. H., & Kustas, W. P. (2008). Daily
   evapotranspiration estimates from extrapolating instantaneous airborne remote
   sensing ET values. *Irrigation Science*, *27*(1), 67-81.

Courault, D., Seguin, B., & Olioso, A. (2005). Review on estimation of
   evapotranspiration from remote sensing data: From empirical to numerical
   modeling approaches. Irrigation and Drainage systems, 19(3-4), 223-249.

DeJonge, K.C., Taghvaeian, S., Trout, T.J., Comas, L.H., 2015. Comparison of canopy
   temperature-based water stress indices for maize. Agric. Water Manag. 156, 51 –
   62. https://doi.org/10.1016/j.agwat.2015.03.023.

Evans, R.G., LaRue, J., Stone, K.C., King, B.A., 2013. Adoption of site-specific variable
   rate sprinkler irrigation systems. Irrig. Sci. 31 (4), 871–887.https://doi.org/10.
   1007/s00271-012-0365-x.

Evett, S. R., Colaizzi, P. D., Lamm, F. R., O'Shaughnessy, S. A., Heeren, D. M., Trout,
   T. J., ... & Lin, X. (2020). Past, present, and future of irrigation on the US Great
   Plains. *Transactions of the ASABE*, *63*(3), 703-729.

Han, M., Zhang, H., DeJonge, K. C., Comas, L. H., & Gleason, S. (2018). Comparison of

three crop water stress index models with sap flow measurements in

maize. *Agricultural Water Management*, *203*, 366-375.

Idso, S. B., Jackson, R. D., Pinter, J. P. J., Reginato, R. J. and Hatfield, J. L. (1981)

Normalizing the stress-degree-day parameter for environmental variability. Agric.

Meteorol., 24, 45-55.

Irmak, S., Haman, D.Z., Bastug, R., 2000. Determination of crop water stress index for

irrigation timing and yield estimation of corn. Agron. J. 92, 1221 – 1227.

https://doi. org/10.2134/agronj2000.9261221x.

Jackson, R. D., Idso, S. B., Reginato, R. J. and Pinter, P. J., Jr. (1981) Canopy

temperature as a crop water stress indicator Wheat. Water Resources Research,

17, 1133-1138.

Jackson, R. D., Reginato, R. J. and Idso, S. B. (1977) Wheat canopy temperature: a

practical tool for evaluating water requirements. Water Resources Research (USA), 13,

651.

Jones, H. G. (1992) Plants and microclimate : a quantitative approach to environmental

plant physiology, Cambridge University Press, New York, USA.

Kalma, J. D., McVicar, T. R. and McCabe, M. F. (2008) Estimating Land Surface

Evaporation: A Review of Methods Using Remotely Sensed Surface Temperature

Data. Surveys in Geophysics, 29, 421-469.

Kustas, W. and Anderson, M. (2009) Advances in thermal infrared remote sensing for

land surface modeling. Agricultural and Forest Meteorology, 149, 2071-2081.

Kustas, W. P., Alfieri, J. G., Anderson, M. C., Colaizzi, P. D., Prueger, J. H., Evett, S. R., ... & Howell, T. A. (2012). Evaluating the two-source energy balance model using local thermal and surface flux observations in a strongly advective irrigated agricultural area. Advances in Water Resources, 50, 120-133.

Lo, T. H., Rudnick, D. R., Ge, Y., Heeren, D. M., Irmak, S., Barker, J. B., ... & Shaver, T. M. (2018). Ground-based Thermal Sensing of Field Crops and Its Relevance to Irrigation Management. University of Nebraska-Lincoln, Extension.

Maguire, M. S. (2018). An evaluation of unmanned aerial system multispectral and thermal infrared data as information for agricultural crop and irrigation management (Doctoral dissertation, University of Nebraska-Lincoln).

Maguire, M. S. (2021). Leveraging unmanned aerial system remote sensing to inform energy and water balance models for spatial soil water content monitoring and irrigation management.

Meron, M., Tsipris, J., Orlov, V., Alchanatis, V. and Cohen, Y. (2010a) Crop water stress mapping for site-specific irrigation by thermal imagery and artificial reference surfaces. Precision Agriculture, 11, 148-162.

Meron, M., Tsipris, J., Orlov, V., Alchanatis, V. and Cohen, Y. (2010b) Crop water stress mapping for site-specific irrigation by thermal imagery and artificial reference surfaces. Precision Agriculture, 11, 148-162.

Nandan, R., Woo, D. K., Kumar, P., & Adinarayana, J. (2021). Impact of irrigation
scheduling methods on corn yield under climate change. Agricultural Water
Management, 255, 106990.

Neale, C., Jayanthi, H. & Wright, J.L. 2005. Irrigation water management using high
resolution airborne remote sensing. Irrigation and Drainage Systems 19(3/4):
321–336.

O'Shaughnessy, S.A., Andrade, M.A., Evett, S.R., 2017. Using an integrated crop water
stress index for irrigation scheduling of two corn hybrids in a semi-arid region.
Irrig. Sci. 35, 451 – 467. https://doi.org/10.1007/s00271-017-0552-x.

O'Shaughnessy, S.A., Evett, S.R., Colaizzi, P.D., Howell, T.A., 2012. A crop water stress
index and time threshold for automatic irrigation scheduling of grain sorghum.
Agric. Water Manag. 107, 122 – 132.
https://doi.org/10.1016/j.agwat.2012.01.018.

O'Shaughnessy, S.A., Evett, S.R., Andrade, M.A., Workneh, F., Price, J.A., Rush, C.M.,
2016. Site-specific variable-rate irrigation as a means to enhance water use
efficiency. Trans. ASABE 59, 239–249.https://doi.org/10.13031/trans.59.11165.

O'Shaughnessy, S.A., Evett, S.R., Colaizzi, P.D., Andrade, M.A., Marek, T.H., Heeren,
D.M., Lamm, F.R., LaRue, J.L., 2019. Identifying advantages and disadvantages
of variable rate irrigation – an updated review. Appl. Eng. Agric.
https://doi.org/10. 13031/aea.13128. (in press).

Park, S. (2018). *Estimating plant water stress and evapotranspiration using very-high-resolution (VHR) UAV imagery* (Doctoral dissertation).

Park, S., Ryu, D., Fuentes, S., Chung, H., Hernández-Montes, E., & O'Connell, M. (2017). Adaptive estimation of crop water stress in nectarine and peach orchards using high-resolution imagery from an unmanned aerial vehicle (UAV). Remote Sensing, 9(8), 828.

Park, S., Ryu, D., Fuentes, S., Chung, H., O'Connell, M., & Kim, J. (2021). Dependence of CWSI-Based Plant Water Stress Estimation with Diurnal Acquisition Times in a Nectarine Orchard. Remote Sensing, 13(14), 2775.

Payero, J. O., & Irmak, S. (2006). Variable upper and lower crop water stress index baselines for corn and soybean. Irrigation Science, 25(1), 21-32.

Peters, R.T., Evett, S.R., 2008. Automation of a center pivot using the temperature-time-threshold method of irrigation scheduling. J. Irrig. Drain. Eng. 134 (3), 286 – 291. https://doi.org/10.1061/ASCE_0733-9437(2008)_134:3(286)

Rud, R., Cohen, Y., Alchanatis, V., Levi, A., Brikman, R., Shenderey, C., Heuer, B., Markovitch, T., Dar, Z., Rosen, C., Mulla, D. and Nigon, T. (2014) Crop water stress index derived from multi-year ground and aerial thermal images as an indicator of potato water status. Precision Agriculture, 15, 273-289.

Shafian, S., Rajan, N., Schnell, R., Bagavathiannan, M., Valasek, J., Shi, Y., & Olsenholler, J. (2018). Unmanned aerial systems-based remote sensing for monitoring sorghum growth and development. PloS one, 13(5), e0196605.

Seguin, B. and Itier, B. (1983) Using midday surface temperature to estimate daily

evaporation from satellite thermal IR data. International Journal of Remote Sensing, 4, 371.

Singh, J., Heeren, D. M., Ge, Y., Bai, G., Neale, C. M., Maguire, M. S., & Bhatti, S. (2021). Sensor-based irrigation of maize and soybean in East-Central Nebraska under a sub-humid climate. In 2021 ASABE Annual International Virtual Meeting (p. 1). American Society of Agricultural and Biological Engineers.

Sui, R., Yan, H., 2017. Field study of variable rate irrigation management in humid climates. Irrig. Drain. 66, 327–339.https://doi.org/10.1002/ird.2111.

Su, Z. (2002) The Surface Energy Balance System (SEBS) for estimation of turbulent heat fluxes. Hydrology and Earth System Sciences, Vol 6, Iss 1, Pp 85-100 (2002), 85.

Taghvaeian, S., Ch́avez, J.L., Hansen, N.C., 2012. Infrared thermometry to estimate crop water stress index and water use of irrigated maize in northeastern colorado. Remote Sens. 4, 3619 – 3637. https://doi.org/10.3390/rs4113619.

Taghvaeian, S., Comas, L., DeJonge, K.C., Trout, T.J., 2014. Conventional and simplified canopy temperature indices predict water stress in sunflower. Agric. Water Manag. 144, 69 – 80. https://doi.org/10.1016/j.agwat.2014.06.003.

UNL. (1977). Center-pivot irrigation systems in Nebraska. Lincoln, NE: University of Nebraska Remote Sensing Center.

USDA-NASS. (2008). Farm and ranch irrigation survey. In 2007 Census of agriculture. Washington, DC: USDA National Agricultural Statistics Service. Retrieved from

http://www.agcensus.usda.gov/Publications/2007/Online_Highli

ghts/Farm_and_Ranch_Irrigation_Survey/index.php

USDA-NASS. (2019a). Irrigation and water management survey In 2018 Census of

agriculture, Vol. 3, Special studies, Part 1 (AC-17-SS-1). Washington, DC:

USDA National Agricultural Statistics Service.

Woldt, W. E., Frew, E. W., & Meyer, G. (2014). Feeding a hungry world: The potential

for unmanned aircraft systems. XRDS Crossroads: The ACM for Students, 20(3),

24-27. https://doi.org/10.1145/2590599

Woldt, W. E., Neale, C., Heeren, D., Frew, E. W., & Meyer, G. E. (2018). Improving

agricultural water efficiency with unmanned aircraft. Proc. Xponential,

Association of Unmanned Vehicle Systems Int.

Woldt, W.E., Neale, C.M.U., Heeren, D.M., Frew, E., Meyer, G.E., 2018. Improving

agri-cultural water efficiency with unmanned aircraft. In: Association for

Unmanned Vehicle Systems International (AUVSI) XPONENTIAL Trade Show

and Conference. Denver, Colo. 8 pages.

Xia, T., Kustas, W. P., Anderson, M. C., Alfieri, J. G., Gao, F., McKee, L., Prueger, J. H.,

Geli, H. M. E., Neale, C. M. U., Sanchez, L., Alsina, M. M. and Wang, Z. (2016)

Mapping evapotranspiration with high-resolution aircraft imagery over vineyards

using one-and two-source modeling schemes. Hydrology and Earth System

Sciences, Vol 20, Iss 4, Pp 1523-1545 (2016), 1523.

Zhao-Liang, L., Ronglin, T., Zhengming, W., Yuyun, B., Chenghu, Z., Tang, B.,

Guangjian, Y. and Xiaoyu, Z. (2009) A Review of Current Methodologies for

Regional Evapotranspiration Estimation from Remotely Sensed Data. Sensors, 9,

3801-3853.

CHAPTER 2. HIGH-FREQUENCY UNMANNED AIRCRAFT FLIGHTS FOR CROP CANOPY IMAGING DURING DIURNAL MOISTURE STRESS

Abstract

Previous research has used unmanned aerial vehicle (UAV) technology for calculating CWSI (Crop Water Stress Index) values in the context of irrigation timing. Typically, these estimations were taken at one time of day, usually near or shortly after solar noon. A significant limitation with these CWSI values is that the UAV thermal imagery captured at this point in time can be affected by various factors like atmospheric air temperature, sun radiation, wind speed, relative humidity, and other micrometeorological disturbances in the air. In order to address these temporal effects, high-frequency UAV flights were conducted over different daylight hours to analyze and compare the CWSI values to create a better understanding of the crop dynamics to irrigation events. In addition, another stress index which requires fewer input data, the Degrees Above Non-Stressed (DANS), were also compared to CWSI values. This research was carried out at three different field research sites in Nebraska: Two at the Eastern Nebraska Research and Extension Center (ENREC), Mead, NE and one at the Irmak Research Laboratory (IRK) in South Central Agricultural Laboratory (SCAL), Clay Center, NE. All fields were growing soybean with various levels of irrigation and rainfed treatments. A DJI M600 UAV was used with MicaSense RedEdge multispectral camera and a FLIR Duo Pro R thermal camera to capture imagery, flying at an altitude of 400 m above ground level. In addition, local meteorological data and ground-based IRT (Infrared Thermometer) data were collected. In order to calculate CWSI and DANS, a thermal

calibrated linear regression model developed by NU-AIRE Lab, UNL, NE, was also used to improve the accuracy of the thermal imagery data. Both thermal and multispectral imagery was been used to analyze the spatiotemporal dynamics of the crop. According to this study, the range of spatial variability of canopy temperature (as measured by the interquartile range) showed a diurnal pattern and was higher when the canopy had water stress (rainfed treatment). A key aspect of this research is the development of a new threshold prediction model based on the CWSI histogram distribution, that revealed threshold values of soybean crop of approximately 0.49, 0.51, and 0.49, respectively for the three research sites. Moreover, CWSI sensitivity analysis with respect to important meteorological factors like air temperature (0.71, 0.81, and 0.98), relative humidity (0.86, 0.97, and 0.98), solar radiation (0.11, 0.16, and 0.011), and wind speed (0.25, 0.32 and 0.96) is also shown in this research using statistical CWSI approach, were little or no research was conducted before.

2.1 Introduction

The use of unmanned aerial vehicle (UAV) systems in irrigation management has increased rapidly due to its low cost, mobility, and accuracy in estimating crop water needs. With the ability to mount different sensors on these UAV systems, it is easy to capture high-resolution spatial and temporal data to help farmers make timely decisions for irrigation applications. When combined with both ground and remote sensing-based techniques, the amount of water required for the field is greatly reduced, while improving the crop water efficiency. For proper irrigation management, knowing crop waters stress and evapotranspiration rate is essential.

Water stress from crop canopy temperature was originally measured using handheld thermography cameras (Tanner et al., 1963 & Gates et al., 1964). Later, Idso et al., (1981), proposed the first indicator of crop stress, by deriving an empirical method, called crop water stress index (CWSI), using a relationship between leaf-to-air temperature difference and vapor pressure deficit. In the same year, Jackson et al. (1981), developed a theoretical method of calculating the CWSI accounting the divergence between the upper and lower boundaries of canopy-to-air temperature difference using the crop canopy energy balance theory, involving the requirement of more meteorological data to account for variation in climate. Both empirical and theoretical methods have been used by different research for irrigation scheduling in past years (Nielsen, 1990; Yazar et al., 1999; Emekli et al., 2007; O'Shaughnessy et al., 2010; Colaizzi et al., 2012).

Recently, above two approaches are widely being used with the help of infrared thermometers (IRTs), being setup on a single plant or nearly whole field to monitor the crop water stress continuously (Singh et al., 2021; O'Shaughnessy et al., 2017, 2012; Candogan et al., 2013; DeJonge et al., 2015; Irmak et al., 2000; Payero and Irmak, 2006; Peters and Evett, 2008; Taghvaeian et al., 2012). However, even with the use of IRTs in the field, the CWSI estimations can easily be disturbed by meteorological factors and variability over the whole field.

With the advancement of various remote sensing platforms and use of UAVs, several studies on crop water stress have been conducted to further simplify the calculation of CWSI by reducing or eliminating the use of ground-based measurements or IRTs, to make it applicable at field scale (Park et al., 2019; Leinonen and Jones, 2004;

Alchanatis et al., 2010; Fuentes et al., 2012; Berni et al., 2009b; Zarco-Tejada et al., 2012; Bellvert et al., 2014). Thus, a statistical approach of calculating CWSI, was used, based on histogram analysis of canopy temperature (Meron et al., 2010 & Rud et al., 2014) that included in the delineation of canopy pixels and calculating T_{wet} from the lowest 5% of temperature histogram and T_{dry} to be equal to the air temperature (T_{air}) + 5 °C (Irmak, 2002), and found similar correlations between the introduced statistical CWSI approach and traditional CWSI approach. Recently, Park et al., (2017) redeveloped the above statistical CWSI approach that can be adaptable to variability over the whole field by stating, that having a single set of Twet and Tdry values will result in inaccurate estimations of CWSI. He considered employing thersholding of Twet and Tdry for each sub-regions by extracting from the critical values of 99% confidence intervals of canopy temperature distribution. This new approach, does not require any meteorological data and reference surfaces, thereby reducing the complexity of estimating the CWSI spatially. A similar research on cotton was also published emphasizing the effectiveness of this canopy temperature histogram approach in comparison to traditional approach by Bian et al., (2019).

Recently, another common water stress index is being used effectively that requires less inputs. It is the degree above non-stressed canopy (DANS) index. DANS is defined as the difference between the canopy temperature Tc and non-stressed canopy temperature T_{NS}. Several authors have found high correlations between these two indices, CWSI and DANS, being much simpler in water stress estimation (Taghvaeian et al., 2014; DeJonge et al., 2015). Therefore, UAV remote sensing technologies have become

a widely available tool for precision agriculture management and crop water stress identification.

Due to the accuracy of the midday system in assessing CWSI, additional research is required to determine the optimal time of day for this estimation (Santesteban et al., 2017). Past researchers have some made efforts to study the CWSI diurnal variations including data collected in the morning (Zhang et al., 2019; Martnez et al., 2017, & Santesteban et al., 2017). However, for these investigations, the TIR image processing failed due to surface temperatures' poor contrast, or the TIR image processing issues.

Therefore, the objective of this study is to evaluate the diurnal response of plants from early morning till evening, by using UAV equipped thermal and multispectral cameras to observe the dynamic difference in crop water stress requirements using statistical CWSI approach. Specific objectives of the study include –

- Using high-frequency UAS thermal data (canopy temperature, CWSI, and DANS) to identify and characterize the temporal nature of the spatial canopy stress patterns for soybean during the moisture stress period in Eastern Nebraska.

- Predicting the threshold value of CWSI and characterizing the range of water stress level indication as low, moderate and high based on CWSI histogram distribution method, over different daylight hours.

- Perform CWSI Sensitivity analysis using statistical based CWSI approach between common meteorological effects such as air temperature, relative humidity, solar radiation and wind speed.

2.2 Material and Methods

2.2.1 Research Sites Description

This research was conducted over three different field sites with soybean as the main crop. Two of the research fields, ENREC1 and ENREC2, are located at the Eastern Nebraska Research and Extension Center (ENREC) near Mead, Nebraska (Figure 2.1, 2.2) and are being administered for the ongoing Variable Rate Irrigation (VRI) projects involving various treatments using a center pivot irrigation system. The latitude and longitude of the center pivot ENREC1 and ENREC2 are 41° 9'53.32"N, 96°25'49.24"W and 41°10'20.81"N, 96°28'41.67"W respectively. The third site, SCAL, is also equipped with center pivot, latitude 40°34'49.88"N and longitude 98° 7'53.79"W, having a uniform irrigation treatment in 2020, and it is located at Irmak Research Laboratory (IRL), South Central Agricultural Laboratory (SCAL), Clay Center, Nebraska (Figure 2.3). The field sizes of ENREC1, ENREC2, and SCAL were approximately 22.25ha, 17.8ha, and 16.18ac respectively (ESRI ArcMap- Google Earth Hybrid basemap, assessed on October 21, 2020).

2.2.2 Experimental Design

2.2.2.1 ENREC1

The ENREC1 field consisted of total 69 experimental plots involving six different irrigation treatments and one rainfed treatment (Figure 2.1) for soybean in the 2020 growing season. The design of these study was a generalized randomized complete block design (RCBD) and treatments were randomly assigned to each plots. The specific treatments were – Common (C) – 11 plots, Rainfed (R) – 12 plots, Uniform (U) – 11

plots , SETMI using satellite (SAT) – 12 plots, SETMI using unmanned aircraft systems (UAS) – 12 plots, and private company treatment (L) – 11 plots. The Common (C) treatment was meant to represent common or conventional practice, with irrigation scheduling based on input from a professional crop consultant together with the farm manager (Maguire., 2021). The Spatial Evapotranspiration Modeling Interface (SETMI) was used for the SAT and UAS treatments (Maguire., 2021), which implemented variable rate irrigation prescriptions. The uniform (U) treatment applied uniform rate irrigation based on stationary sensors (Singh et al., 2021). For Rainfed treatment plots, no irrigation was applied for this study. Bhatti et al. (2020) and Barker et al. (2018) provide more information about these treatments in detail.

2.2.2.2 ENREC2

ENREC2 field site consisted of total 48 experimental plots with four different irrigation treatments (Figure 2.2) for soybean in the 2020 growing season (Bhatti et al., 2021). The complex experimental design block consisted of 8 rings assigned radially from inside to outside, consisted of each treatment repeated twice randomly. The field was divided into six sectors, resulting in 6 plots in each ring. The four irrigation treatments include percentage of irrigation applied with description as – 0% or Rainfed – 12 plots, 50% or Deficit – 12 plots, 100% or Full – 12 plots, and 150% or Over – 12 plots. Here, Rainfed plots had no irrigation applied for this study.

2.2.2.3 SCAL

SCAL field is a part of Irmak Research Laboratory, SCAL, Clay Center, NE. It consisted of a uniform irrigation treatment throughout the whole soybean field for 2020

growing season (Figure 2.3). Irmak and Mutiibwa. (2009) report long-term maximum and

minimum air temperatures of 25°C and 5°C, respectively. The research field consisted of

three soil types: (i) Cretan silt loam, 0–1% slope [soil 1 (S1)], (ii) Hastings silty clay

loam, 3–7% slope [soil 2 (S2)] and (iii) Hastings silt loam, 1–3% slope [soil 3 (S3)] (Fig.

1) (Sharma & Irmak, (2021)).
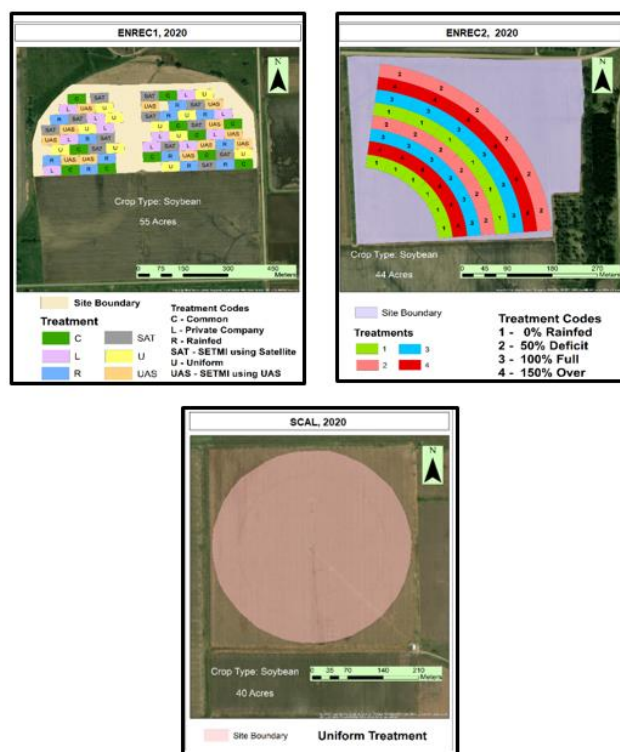
Figure 2. 1 (Top Left): Study Site ENREC1 (55ac) of 2020 growing season with Soybean. The experiment design has six different treatments. Located at Eastern Nebraska Research and Extension Center (ENREC) near Mead, NE. Background basemap: World Imagery from ESRI ArcMap.
Figure 2. 2 (Top Right): Study site ENREC2 (44ac) of 2020 growing season with Soybean. The experiment design has four different treatments. Both sites are located at Eastern Nebraska Research and Extension Center (ENREC) near Mead, NE. Background basemap: World Imagery from ESRI ArcMap.
Figure 2. 3: Study SCAL (40ac) from Irmak Research Laboratory (IRL) located at South Central Agricultural Laboratory (SCAL), Clay Center, NE. Crop: Soybean. Uniform irrigation treatment of 2020 growing season. Background basemap: World Imagery from ESRI ArcMap.

2.2.2 Data Acquisition

The data collected in this study includes using a UAS (a six-rotor DJI Matrice 600, manufactured by DJI, Inc., USA), a Thermal Infrared (TIR) sensor (FLIR Duo Pro R, FLIR System, Inc., USA), and a multispectral sensor (MicaSense RedEdge, MicaSense, Inc., USA) (Figure 2.4). The characteristics of the DJI M600 includes maximum payload of 15.1kg, withstanding of maximum wind speed of 8 m/s, and an average flight time of 17 minutes. The Uncooled VOx Microbolometer TIR sensor has a spatial resolution of 640 x 512 pixels, a spectral range of 7.5 to 13.5 μm, a focal length of 13 mm, a thermal sensitivity of 50 mk, an image angle of 25° (H) × 20° (V), and with a GSD of 15.5 cm/ pixel at 120 m AGL (Table 2.1). The MicaSense Rededge multispectral sensor consisted of five bands with spectral ranges at 475, 560, 668, 840 and 717 nm, at a spatial resolution of 1280 x 960 pixels, a fixed 5.5 mm lens, a horizontal viewing angle of 47.2°, and having Ground Sample Distance (GSD) of 8.2 cm/pixel at 120 m AGL (Table 2.2). Original MicaSense calibrated reflectance panel was used before and after each flights for accurate data collection (Figure 2.4). These multispectral and thermal images was collected using the UgCS Flight Mission Planning software (UgCS, USA) with a 90% front overlap and a 60% side overlap at an altitude of 400 ft (120 m AGL). After the data collection, all the images were processed using Pix4Dmapper (Pix4D, USA) to generate ortho-mosiacs and corrections for image vignetting and bidirectional reflectance effects (Maguire et al., 2018).

This research involved 50 flight missions (17-ENREC1, 20-ECNREC2, 13-SCAL) in total, over the three different fields, in the 2020 growing season at full canopy

(August, 2020 till September, 2020) for analysis. During the processing of these data sets, several issues had been identified while image stitching process (Appendix). Detail description of these errors, and failure to use several images in the analysis has been described in Chapter 3. Nevertheless, from the total 50 flights, the success rate of obtaining good thermal and multispectral dataset was 86% and 48%, respectively.

For the current research, the study had selected 11 successful datasets for identifying the diurnal moisture stress within each field. Local meteorological data for the fields ENREC1 and ENREC2 are obtained from High Plains Regional Climate Center's Agricultural Weather Data Network's (AWDN) Mead Agronomy Farm weather station. For SCAL, High Plains Regional Climatic Center- Automated Weather Data Network (HPRCC-AWDN) was obtained. Specific dates and time of the UAV flight campaign along with specific meteorological data like air temperature, relative humidity, and wind speed at the time of flights are shown in Table 2.3.

Figure 2. 4. DJI Matrice 600 attached MicaSense Rededge multispectral and FLIR Duo Pro R thermal sensors (Left) and MicaSense calibration redlectance planel (Right).

Table 2. 1. FLIR Duo Pro R Thermal camera specifications.

Spectral Band	7.5-13.5 µm
Thermal Frame Rate	30 Hz
Thermal Imager	Uncooled VOx Microbolometer
Focal Length	13 mm
Field of View	45° x 37°
Thermal Sensitivity	<50 mK
Thermal Sensor Resolution	640 x 512
Ground Sampling Distance	3.2 cm/pixel at 120 m AGL
Measurement Accuracy	+/- 5 °C or 5% of readings in the -25°C to +135°C range +/- 20 °C or 20% of readings in the -40°C to +550°C range

Table 2. 2. MicaSense RedEdge multispectral camera specifications.

Band Name	Center Wavelength (nm)	Bandwidth FWHM (nm)
Blue	475	20
Green	560	20
Red	668	10
Near IR	840	40
Red Edge	717	10
Ground Sampling Distance		8.2 cm/pixel at 120 m AGL
Lens Focal Length (mm)		5.5
Lens Field of View (degrees HFOV)		47.2
Image Resolution (pixels)		1280 x 960

Table 2. 3. UAV Flight Campaign with time specific meteorological data

Plot	Date	Time	Temp °C	RH %	Wind Speed (m/s)
ENREC #2092	08/26/2020	11:30 AM	31.18	44.25	5.12
		02:30 PM	33.84	34.55	5.16
		04:30 PM	33.84	30.17	5.03
		07:00 PM	28.59	51.54	1.8

ENREC #2436	08/26/2020	10:30 AM	29.01	52.61	3.83
		01:30 PM	33.51	36.12	5.13
		03:45 PM	33.83	34.01	5.09
		06:00 PM	31.73	38.05	3.09
SCAL CP-1	08/28/2020	11:00 AM	27.66	73.75	2.89
		01:30 PM	28.9	67.94	3.04
		04:00 PM	31.05	58.85	3.37

2.2.3 TIR Image Correction and Calibration

Multispectral reflectance and thermal infrared cameras are two common sensors used in agricultural remote sensing. In order to maintain measurement accuracy, thermal camera sensors are often cooled to a specific temperature. Typically, uncooled microbolometer thermal cameras are used in most research since they are compact and light. As a downside to an uncooled sensor, it's less accurate and sensitive in thermal measurements, as microbolometers can cause changing temperatures in the camera body and sensor. To account for this temperature inaccuracy, thermal image corrections are applied (Maguire., 2021).

Maguire., 2021, in his study, used two levels of corrections on thermal imagery, one for emissivity and other for atmospheric interference. Generally, for vegetation and crop canopy, existing literature has provided an emissivity value of 0.98 and for soils it is 0.96 (Chen, 2015). For TIR correction of emissivity, two critical factors are considered, that are the surface temperature being measured and degree of correction with respect to the variance between the set camera emissivity and actual surface emissivity. The TIR images are needed to be corrected by relying on the actual surface emissivity as compared to the surface being imaged (crop canopy).

A review of literature related to the computation of emissivity has provided

several methods from a multi-spectral reflectance imagery perspective, by Brunsell and

Gillies in Maguire (2021). The method involves into the consideration of the percentage

canopy cover derived from NDVI to compute its weighted emissivity value for vegetation

and soil. The percentage of cover using NDVI was computed as illustrated in equation

2.1 below

$$f_c = ((NDVI - NDVI_{min})/ (NDVI_{max} - NDVI_{min}))^2 \qquad (2.1)$$

where $NDVI_{min}$ and $NDVI_{max}$ represent the $NDVI$ values of bare soil and full

crop canopy cover, while $NDVI$ represented as the computed surface NDVI.

Following the recommendations provided by Li et al. in Maguire (2021), the

$NDVI_{min}$ and $NDVI_{max}$ values for bare soil and crop canopy cover were adopted as 0.1

and 0.89 respectively. The actual emissivity was then computed using equation 2.2

below:

$$Emissivity\ (\varepsilon)\ =\ fc * 0.98 + (1 - fc) * 0.96 \qquad (2.2)$$

where fc represents a percent of crop cover.

Secondly, In order to achieve atmospheric interference correction to TIR thermal

images, additional measures were considered by the study. With respect to the prevailing

atmospheric conditions, the thermal signals were enhanced to improve the sensitivity and

accuracy of the cameras. The atmospheric values were computed with the assistance of

the online atmospheric profile calculator as provided by Barsi et al. in Maguire (2021)

that took into consideration of space and time of particular imagery collected. These

values were weighed, summed and used to compute the atmospheric interference

affecting TIR thermal image over the spectral responses of the thermal camera with an

IRT corrected measurements using Planck's equation.

A review of literature has provided three different methods of computing correction in atmospheric interference by taking into consideration the variation in the set targets and the actual surface emissivity (Maguire, 2021). These methods include i) linear model, as illustrated in equation 2.3 below, ii) the second order polynomial, and iii) artificial neural network. Although these models have adopted the same parameters such as UAS non-corrected surface temperature measurements (UAS), modeled surface emissivity (ε), and atmospheric pressure (P), air temperature (Tair), and relative humidity (RH) measured at the time of UAS flights, this study narrows down to using a linear model.

$$\text{IRT}_{\text{atm}} = \beta_0 + \beta_1 \text{UAS} + \beta_2 \text{T}_{\text{air}} + \beta_3 \text{RH} + \beta_4 \text{P} + \beta_5 \varepsilon \qquad (2.3)$$

where $\beta_0, \beta_1, \beta_2, \beta_3, \beta_4,$ and β_5 are the coeifficents of linear model, IRT$_{\text{atm}}$ is the IRT atmposphere corrcetd surface temperature, UAS is the non-corrected or raw surface temperature from TIR Imagery, T$_{\text{air}}$ is the air temperature, RH is relative humidity, P is the atmospheric pressure and ε is the modeled surface emisiivity calculated using the above equation (2.2).
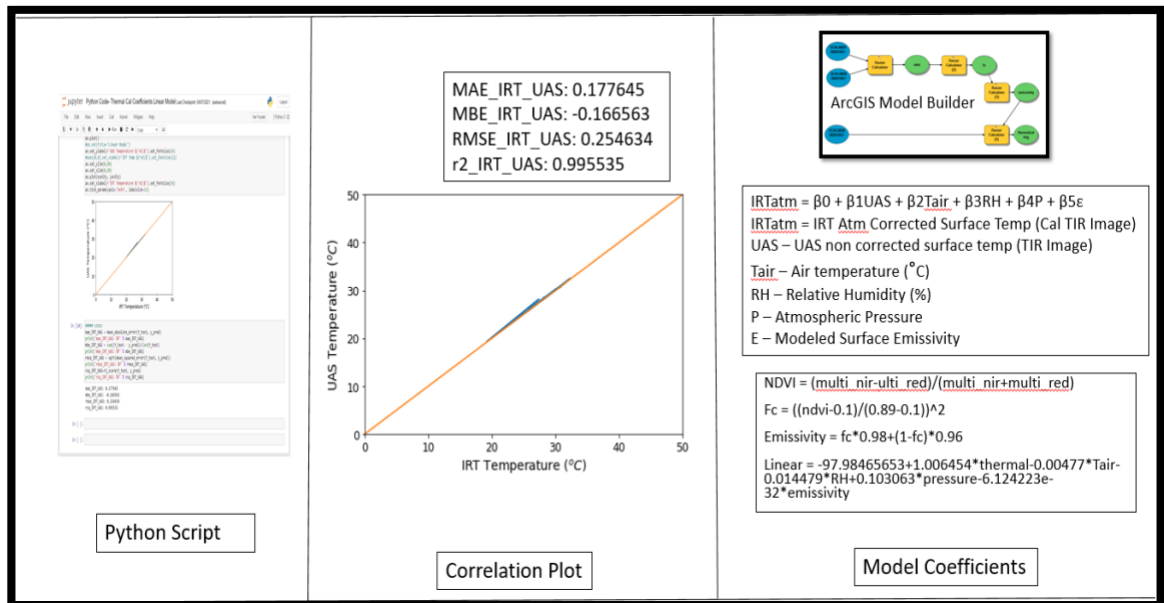
Figure 2. 5 Workflow of linear thermal calibration. (Left) Python script- includes training data of UAS temperature, corrected IRT temperature, and meteorological data. (Middle) Correlation plot between UAS and IRT temperature. (Right) Linear thermal calibration model equation and ArcGIS Model Builder inputs.

The whole linear regression analysis is done using a Python script on Jupiter Notebook platform by training model dataset. As a result the correlation plot between UAS Temperature (°C) and IRT Temperature (°C) resulted a positive correlation with determinent coiefficent (r2) of 0.99, RSME of 0.254, MAE of 0.177 and MBE of 0.17. The model coefficient outputs where β0= -97.98465653, β1=1.006454, β2=-0.00477, β3=-0.014479, β4=0.103063, β5= -6.124223e*32. After analyzing high correlation between UAS temperature and IRT temperature predicted by the training model, an assumption was made that the thermal imagery had less disturbance in the canopy temperature range with the flights made at 120 m AGL. Despite having high correlations, all the Thermal raw imagery were processed using thermal calibrated linear model using ArcGIS Model Builder (ESRI, ArcGIS, USA).

2.2.4 CWSI, DANS and Spectral Indices

2.2.4.1 CWSI Calculation

The CWSI (Crop Water Stress Index) temperature-based Index was developed by (Idso et al., 1981).

$$CWSI = \frac{T_c - T_{wet}}{T_{dry} - T_{wet}}$$ (2.4)

Where T_c is the canopy temperature after removal of soil pixel on the thermal calibrated images, T_{wet} is the temperature of a fully transpiring leaf or lower reference, and T_{dry} is the temperature of a non-transpiring leaf, also considered as upper reference.

2.2.4.2 DANS Calculation

Recently several authors published and used a new index, DANS (Degrees Above Non Stressed) that require fewer inputs (DeJonge, 2015). It is defined as the difference between canopy temperature and the non-stressed crop. In our case, the non-stressed crop in the TIR refers to the temperature of a fully transpiring leaf $T_{wet.}$

$$DANS = T_c - T_{NS}$$ (2.5)

Where T_c is the canopy temperature after removal of soil pixel on the thermal calibrated images and T_{NS} is the temperature of the non-stressed crop or fully transpiring leaf.

2.2.4.3 T_{wet} and T_{dry} Extraction from TIR Imagery

As discussed in the introduction, many studies used different methods to calculate T_{wet} and T_{dry} values (Table 2.4). In this study, the CWSI and DANS index is being calculated using the statistical method developed by Park in his research paper (Park, 2017), for the extraction of T_{wet} and T_{dry} values using a TIR imagery. This approach

greatly reduces the complexity involved in the calculation of CWSI. In particular, there

would be no use of any meteorological data or reference surfaces, and the values can be

estimated purely based on the collected thermal imagery. The general tools required for

the extraction of T_{wet} and T_{dry} values from the soybean canopy involves:

1. MATLAB for Canny Edge Detection.

2. Python environment and various python libraries.

3. Excel for storing T_{wet} and T_{dry} values.

Table 2. 4. Methods to calculate T_{wet} and T_{dry} values

Value	Method	Reference
T_{wet}	Non Water Stress Baseline (NWSB) – Linear Regress Function between difference in canopy and air temperature, and vapor pressure deficit (VPD).	(Jackson et al., 1981)
	Wet Artificial Reference Surface (WARS) acting as fully transpiring crop.	(Meron et al., 2013)
	Canopy histogram method (lowest 5%)	(Rud et al., 2014; Poblete-Echeverría et al., 2016)
T_{dry}	Dry reference lead coated with petroleum jelly.	(Jones, 1999)
	(Tair) + 5 ∘C	(Irmak et al., 2000; Cohen et al., 2005; Rud et al., 2014; López-López et al., 2011)
	Histogram analysis of canopy temperature	Rud et al. (2014)

In detail, a temperature histogram was generated from a TIR image using a

Python script that created a bimodal density distributions of temperature values,

representing canopy and soil pixels. The T_{wet} and T_{dry} calculation requires pure canopy

pixels, and it is necessary to exclude soil and mixed canopy-soil pixels from UAV

thermal imagery. This was done using a Canny edge detection in Matlab R2021a

(Mathworks Inc., Matick, MA, USA). The Canny edge detection uses the brightness

discontinuation principle to identify different objects in an image; different objects have varying brightness reflection properties (Crusiol et al., 2020). Next, the new image loaded into the python and fit with a Gaussian Mixture Model (GMM) to objectively cluster canopy and soil mixed pixels. Later, the T_{wet} can be taken as the mean value of the lowest 0.5% of the temperature distribution histogram assuming as a fully transpiring leaf, and the T_{dry} can be taken as the mean value of the highest 0.5% of the temperature distribution histogram assuming as a non-transpiring leaf. Thus, the two-sided critical values at the 1% and 99% confidence interval (CI) of canopy temperature histograms were considered for each TIR imagery for the extraction of multiple T_{wet} and T_{dry} values.
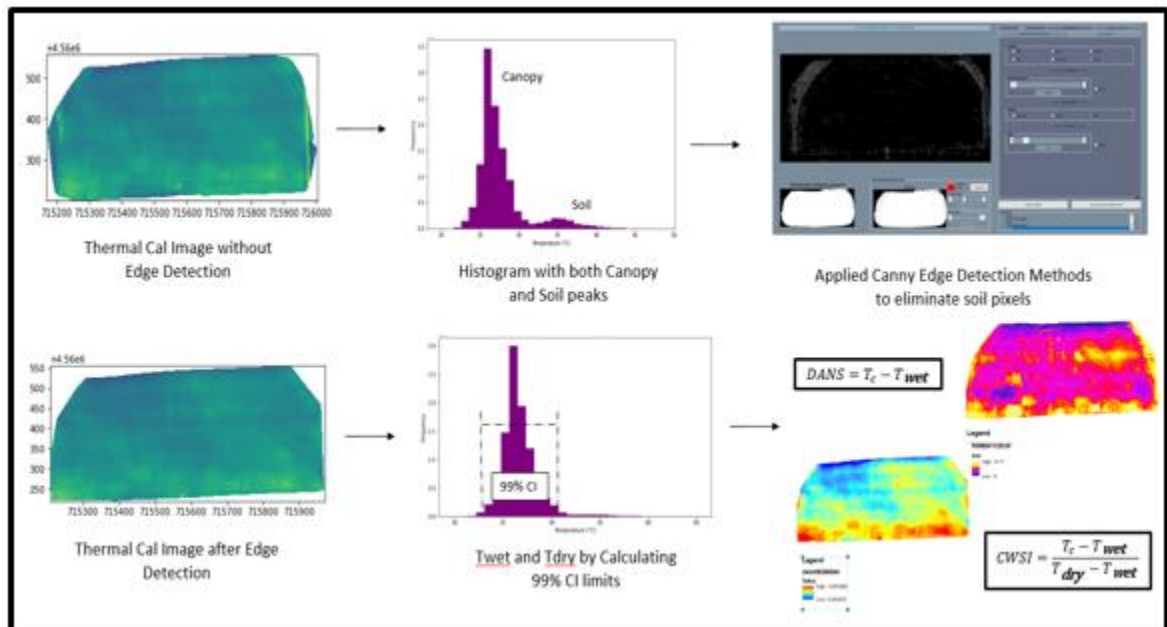
Figure 2. 6. Workflow of Twet and Tdry values extraction from a thermal calibrated image for furthur calculations of CWSI and DANS index. Steps include: Creation of bimodal histogram (canopy and soil pixels) of temperatures from the study site thermal image. Applying Canny edge detection menthos to eliminate soil and mixed canopy soil pixels. Re-creation of temperature histogram. Extracting Twet and Tdry values from two sided critical values of 99% CI of temperature histogram.

2.2.4.4 NDVI Calculation

Normalized Difference Vegetation Index (NDVI) is defined as the difference

between near-infrared and red bands to the ratio of near-infrared plus red, taken from

multispectral sensor. The near-infrared band is used for reflecting vegetation effectively,

whereas red band absorbs vegetation. Combination of both these bands is used to

quantify vegetation within the imagery.

$$NDVI = \frac{NIR - \text{Red}}{NIR + \text{Red}} \tag{2.6}$$

where NIR is near-infrared light and Red is visible red light. It values ranges

between -1 and +1. However, it can be different for different land cover type. Usually

NDVI is calculated at the early in crop season. It shows the variation in chlorophyl and

plant density. Over time in later crop growth stages, these values gets saturated and are

less useful.

2.2.4.5 NDRE Calculation

Normalized difference Red Edge (NRDE) is defined as the difference between

near-infrared and red edge bands to the ratio of near-infrared plus red edge bands, taken

from multispectral sensor. Similar to NDVI, both near-infrared and red edge bands are

used to indicate vegetation effectively.

$$NDRE = \frac{NIR - \text{RE}}{NIR + \text{RE}} \tag{2.7}$$

Where NIR is near-infrared light and RE is the red-edge light. It values also

ranges between -1 to +1. However, NDRE gives a better indicator of vegetation cover

during the mid to late crop growth stages. Red edge band is more translucent than the red

bands to absorb canopy when its dense and better for biomass estimation.

2.3 Results

2.3.1 CWSI, DANS and VI Maps

This section presents CWSI, DANS and VI maps (Figure 2.6 to 2.8) developed

from the TIR and multispectral imagery using equations 2.4 to 2.7. A summary of

statistical data that was extracted from TIR imagery using Python script (Table 2.5) is

shown below. With a 99% confidence interval, Twet and Tdry thresholds are calculated

from the GMM model output on canopy temperature histogram. The different mean and

SD values in the table indicate that the distribution of canopy temperatures can vary

between different times of a day even under different irrigation treatments. Based on the

results obtained, it is noted that ENREC2 achieved the highest mean temp as compared to

SCAL and ENREC1.

Table 2. 5. Summary Statistics for canopy temperature (°C) extracted
from TIR Imagery

| Plot | Date / Time | Mean | SD | 99% CI | |
				Twet	Tdry
ENREC1	8/26/2020 11:30	26.69	1.51	22.8	30.58
ENREC1	8/26/2020 14:30	29.95	1.79	25.33	34.56
ENREC1	8/26/2020 16:30	28.7	1.5	24.83	32.57
ENREC1	8/26/2020 19:00	24.44	1.28	21.13	27.75
ENREC2	8/26/2020 10:30	26.55	2.27	20.69	32.41
ENREC2	8/26/2020 13:30	32.4	2.63	25.61	37.56
ENREC2	8/26/2020 15:45	32.52	2.37	26.4	38.64
ENREC2	8/26/2020 18:00	28.43	1.9	23.52	33.34
SCAL	8/28/2020 11:00	24.36	0.61	22.78	25.95
SCAL	8/28/2020 13:30	29.92	1.28	26.61	33.22
SCAL	8/28/2020 16:00	28.42	1.04	25.72	31.12

The below water stress and VI maps show that there are noticeable differences

among the experimental plots of ENREC1, ENAREC2 and SCAL field sites. These maps

indicate that there are strong indications of observing diurnal water stress conditions. The following high-resolution maps is only a sample representation of flights taken on August 26, 2020 for ENREC1 and ENREC2 and on August 28, 2020 for SCAL. Remaining maps on different times of UAV Campaign are show in Appendix section.

According to the four different flights at ENREC1 and ENREC2 on 26th August, and three different flights at SCAL taken on 28th August of 2020 growing season, the stress patterns in different treatments had significant differences at different times. On the whole plot, the intensity or variation in color range changes from less stress to high stress during the morning till late afternoon, and to a less stress patterns later in the evening for CWSI and DANS maps. In terms of pixel resolution, each pixel had a size roughly equivalent to a thermal image of 15 x 15 cm. Since NDVI and NDRE are less sensitive to the temporal flights and indicate the plant health status only one set of flights has been shown from figures 2.7-2.9.
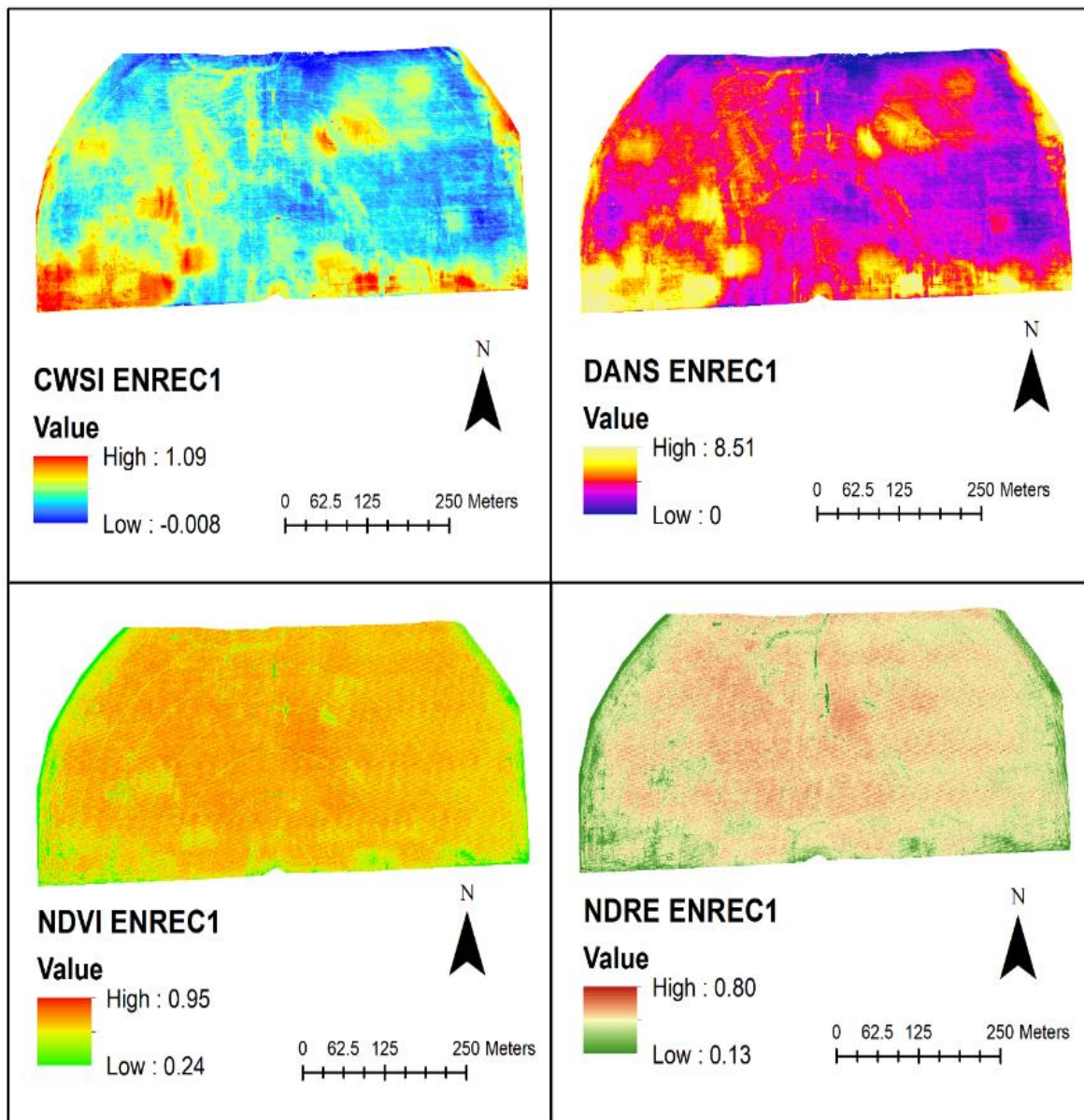
Figure 2. 7 (Top-Left) CWSI maps developed using statistical approach shows CWSI ranges from -0.008 to 1.09. (Top-Right) DANS map ranging from 0 to 8.51. (Bottom-Left) NDVI ranges from 0.24 to 0.95. (Bottom-Right) NDRE ranges from 0.13 to 0.80. Study site: ENREC1, Mead, NE. Maps developed using ESRI ArcMap for 26th August, 2020 at 2:30 PM.
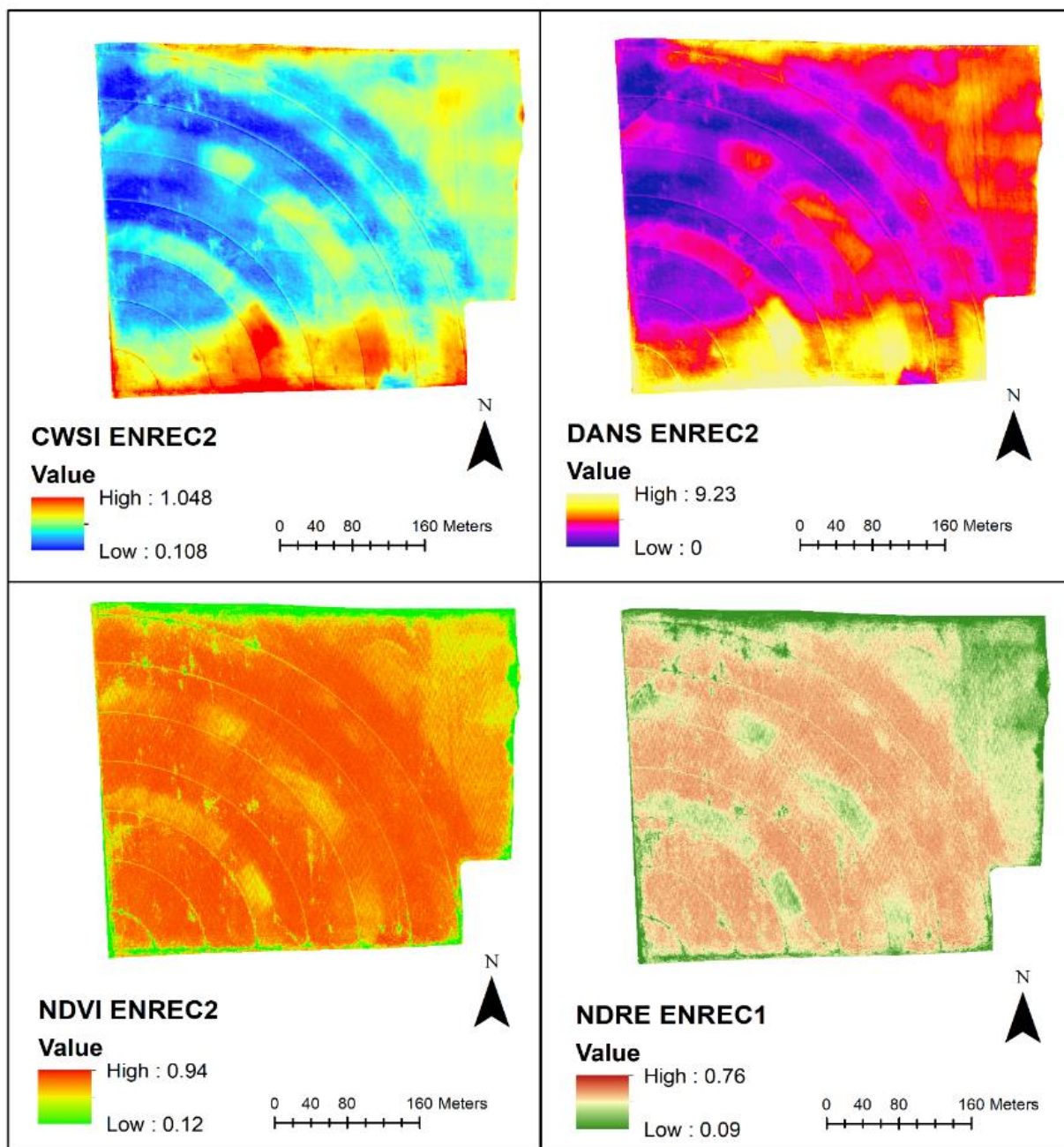
Figure 2. 8 (Top-Left) CWSI maps developed using statistical approach shows CWSI ranges from -0.108 to 1.048. (Top-Right) DANS map ranging from 0 to 9.23. (Bottom-Left) NDVI ranges from 0.12 to 0.94. (Bottom-Right) NDRE ranges from 0.09 to 0.76. Study site: ENREC2, Mead, NE. Maps developed using ESRI ArcMap for 26th August, 2020 at 1:30 PM.
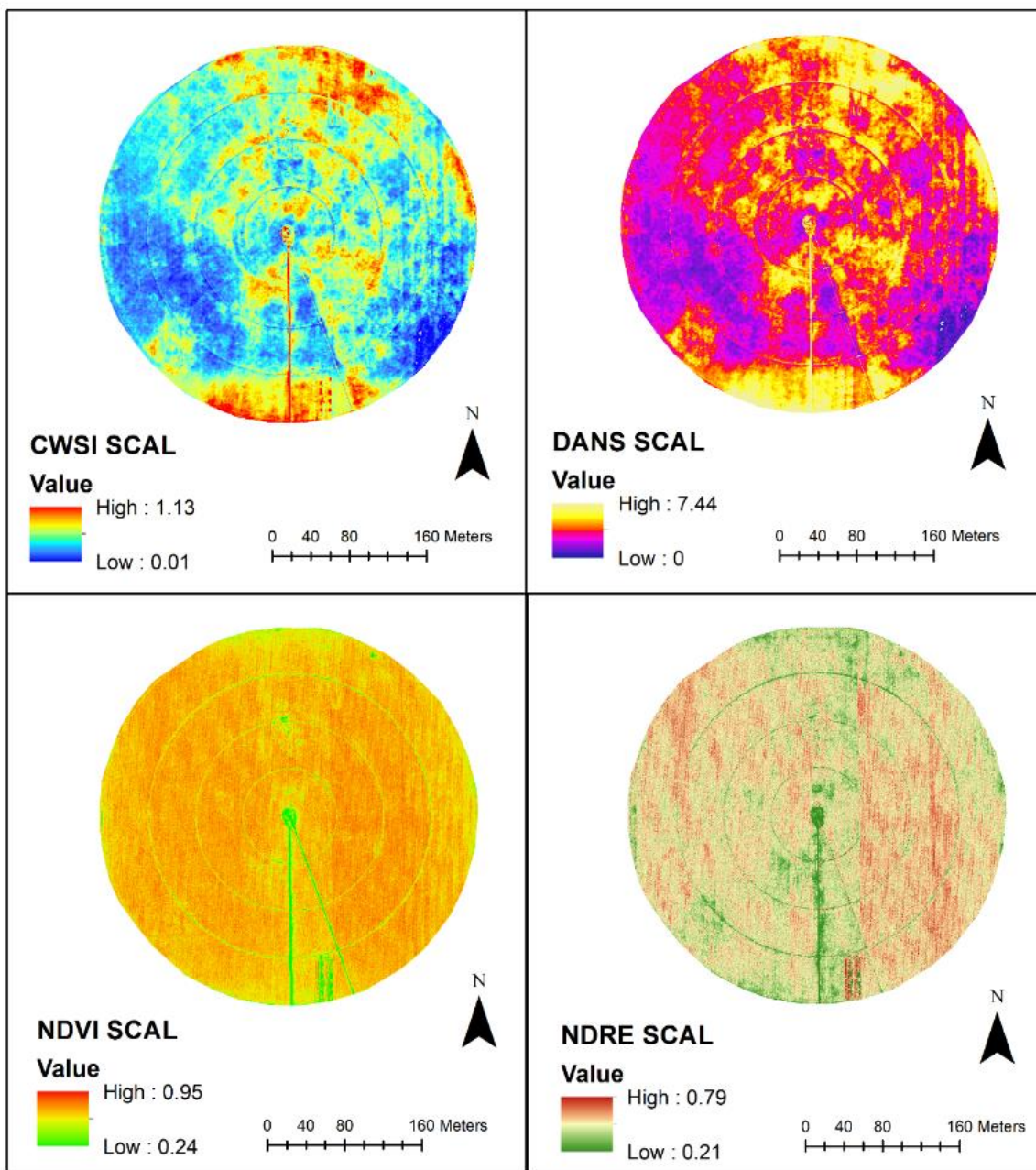
Figure 2. 9 (Top-Left) CWSI maps developed using statistical approach shows CWSI ranges from -0.01to 1.13. (Top-Right) DANS map ranging from 0 to 7.44. (Bottom-Left) NDVI ranges from 0.24 to 0.95. (Bottom-Right) NDRE ranges from 0.21 to 0.79. Study site: SCAL, Clay Center, NE. Maps developed using ESRI ArcMap for 28th August, 2020 at 1:30 PM.

2.3.2 Diurnal Temperature differences

The diurnal temperature differences for the selected three different field sites (ENREC1, ENREC2, and SCAL) are shows below from figure 2.10 to 2.12. Delta T (ΔT) represents the difference between crop canopy temperature (Tc) and the air temperature (Ta), to determine the level of water stress in plants. The value of (Tc) is calculated as the averaged canopy temperature value taken from each different treatment for each flight time, and (Ta) are the air temperature values taken from nearby AWDN weather station during each flight time.
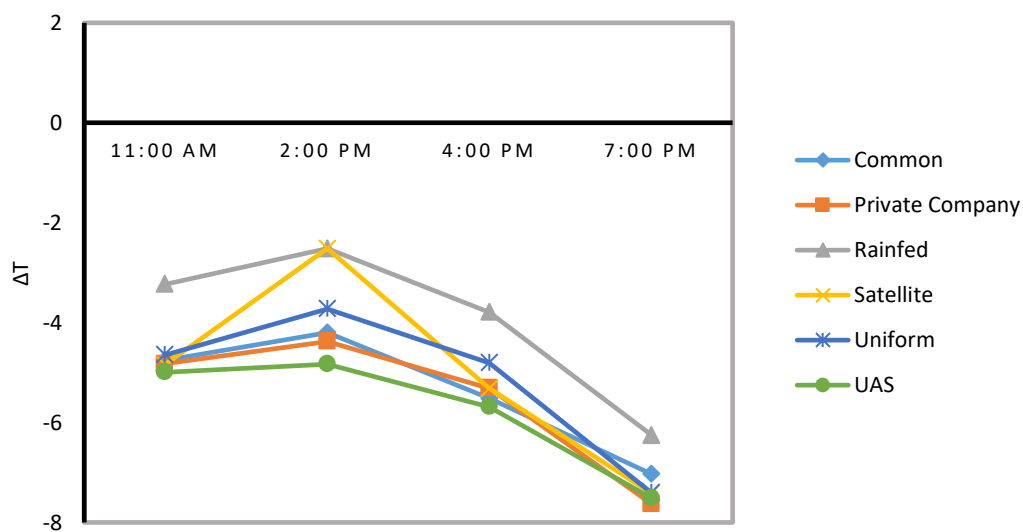
Figure 2. 10 Difference between Canopy and air temperature (ΔT) for study site ENREC1, over a day. Treatments involved are Common, Rainfed, Private Company, SETMI using Satellite, SETMI using UAS, and Uniform treatments. The trends show an increase in (ΔT) from morning till afternoon and drops significantly afternoon till evening.
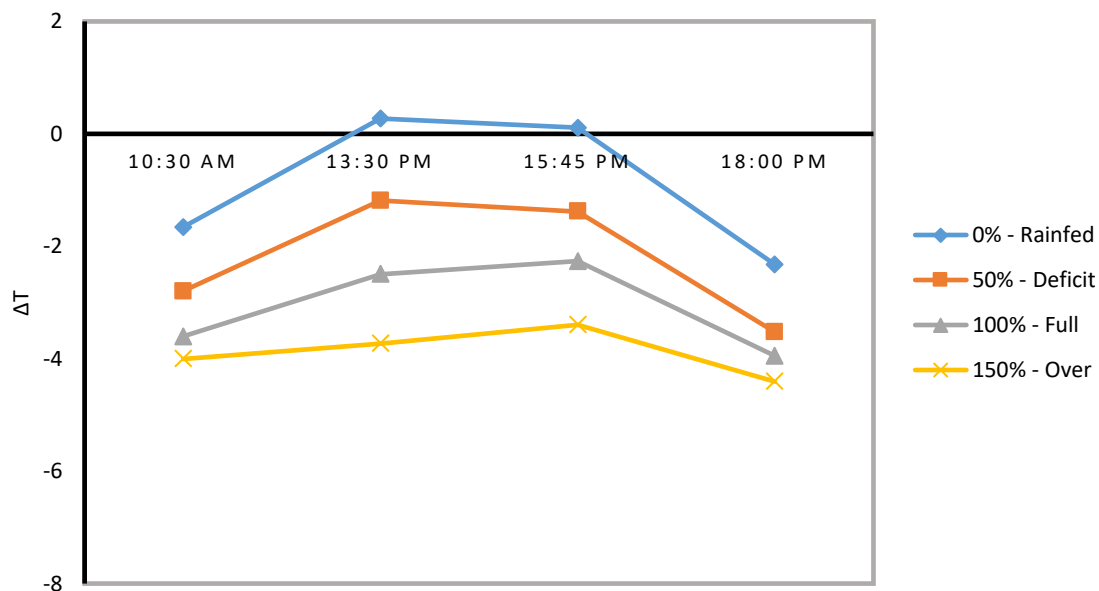
Figure 2. 11 Difference between Canopy and air temperature (ΔT) for study site ENREC2, over a day. Treatments involved are Rainfed, Deficit, Full and Over Irrigation treatments. The trends show an increase in (ΔT) from morning till afternoon and drops significantly afternoon till evening.
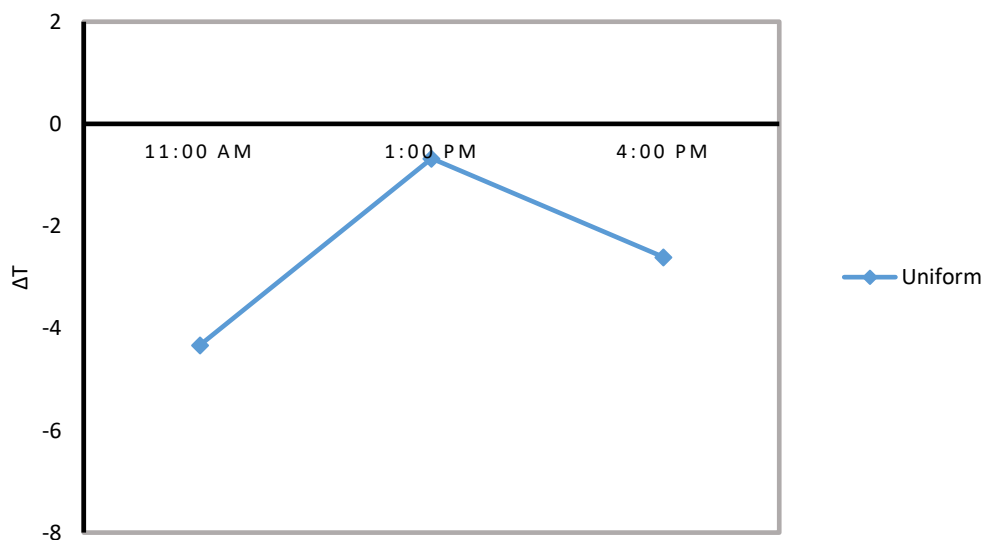
Figure 2. 12 Difference between Canopy and air temperature (ΔT) for study site SCAL, over a day. Uniform irrigation treatment applied. The trends show an increase in (ΔT) from morning till afternoon and drops significantly afternoon till evening.

The results for the study on ENREC1 (Figure 2.10), represents (ΔT) taken at four times in a day on August 26th 2020. The line plot shows crop stress response and recovery from morning till late afternoon for six different treatment plots within the field. The rainfed (R) and satellite (SAT) treatment plots in the field clearly stands out indicating higher water stress as compared to other treatments. The UAS plots in the field is assumed to have the least water stress and having sufficient water in the plots, as per the results obtained. However, all treatments plots followed a similar pattern, i.e., having a warmer canopy temperature in the morning (11 AM) and cooler temperatures during the evening (7 PM). The time period between morning and afternoon (2 PM) showed a constant increase in the canopy temperature due to increase in its surrounding air temperature and maintained the stress until slowly dropping at later afternoon (4 PM) as air temperature drops significantly.

Similar to the study done of ENREC1, the ENREC2 plots (Figure 2.11) which are located within one mile radius to ENREC1, is observed to have similar trends in water stress patterns from morning till evening, but the range of (ΔT) is much higher in this field. The Rainfed (R) treatment plots in ENREC2 indicate higher water stress, i.e., greater that $0°C$ in (ΔT) during afternoon time period, indicating that the canopy temperature was much higher than that of air temperature. The Over (150%) irrigation plots is expected to have the least water stress as compared to Full (100%) and deficit (50%) plots at ENREC2.

The SCAL (Figure 2.12) field plot consists of only uniform irrigation treatment. The (ΔT) trends in this field site displayed similar patterns in increasing water stress from morning (11AM) till afternoon (2 PM), but there is a significant drop during late afternoon hours (4 PM) when compared with other two field sites at same time. The air temperature at this location was cooling faster, resulting in the canopy losing its warmth rapidly.

In addition to (ΔT) trends, this study also extracted a descriptive statistic for each flight using a Python code. It includes mean, standard deviation, first and third quartile, and the interquartile range (IOR) for ΔT after removing the soil and canopy pixels. Tables 2.6 and 2.7 presents a comparison between rainfed treatment and uniform/ full treatment obtained from ENREC1 and ENREC2.

Table 2. 6 Summary Statistics Extracted from ΔT for ENREC1 for rainfed and uniform treatments after removing soil and mixed soil-canopy pixels

Treatment	Date/ Time	ΔT (°C) min	ΔT (°C) max	Mean	Std	Q1	Q3	IQR
Rainfed	8/26 11:00	-5.90	0.26	-3.721	1.08	-4.66	-2.792	1.86
	8/26 14:00	-6.12	1.53	-2.622	1.38	-3.495	-1.528	1.96
	8/26 16:00	-7.36	-1.24	-4.191	1.02	-5.234	-3.414	1.82
	8/26 19:00	-8.58	-4.67	-6.428	0.86	-7.125	-5.691	1.43
Uniform / Full	8/26 11:00	-7.72	-2.90	-5.729	0.85	-6.344	-5.09	1.25
	8/26 14:00	-5.25	0.06	-2.694	0.92	-3.378	-1.943	1.43
	8/26 16:00	-6.98	-2.12	-4.141	0.75	-4.661	-3.62	1.04
	8/26 19:00	-8.85	-6.06	-7.46	0.4	-7.745	-7.211	0.53

Table 2. 7 Summary Statistics extracted from ΔT for ENREC2 for rainfed and uniform treatments after removing soil and mixed soil-canopy pixels

Treatment	Date/ Time	ΔT (°C) min	ΔT (°C) max	Mean	Std	Q1	Q3	IQR
Rainfed	8/26 10:30	-6.45	3.88	-1.66	1.78	-0.811	1.192	2.01
	8/26 13:30	-5.61	4.49	0.28	2.06	-3.727	-1.234	2.49
	8/26 15:45	-5.79	5.23	0.13	1.64	-2.947	-0.612	2.33
	8/26 18:00	-7.11	2.12	-2.31	1.62	-0.881	0.924	1.81
Uniform / Full	8/26 10:30	-6.74	3.88	-3.61	1.56	-1.362	-3.152	1.79
	8/26 13:30	-6.45	5.23	-2.23	1.77	-2.551	-4.561	2.01
	8/26 15:45	-6.99	4.49	-2.48	1.69	-1.698	-3.158	1.46
	8/26 18:00	-7.11	2.12	-3.91	1.54	-1.745	-3.125	1.38

The results revealed that rainfed treatment in both cases provided a higher IQR as compared to the uniform/ full treatment. The information on IQR for different times can also be used as a predictive threshold to quantify the water stress and irrigation application. From Table 2.6 and Table 2.7, it can be predicted that the threshold values of approximately 1.4 and 2, from uniform irrigation treatment can be utilized as the threshold value to trigger irrigation event based on ΔT.

2.3.3 Correlation between CWSI and DANS

Similar to CWSI, soybean DANS maps for each flight were created as an indication of water stress. In general, when DANS values were correlated to CWSI for each flight, the correlation showed a near-perfect linear relationship, which may be expected since both DANS and CWSI were calculated as linear functions of T_c for each pixel. Therefore, the scatterplot was created between CWSI and DANS for all the flight

times at SCAL, ENREC1 and ENREC2 to test to see whether there was a significant

correlation between the two stress indices throughout a day (Figure 2.13).
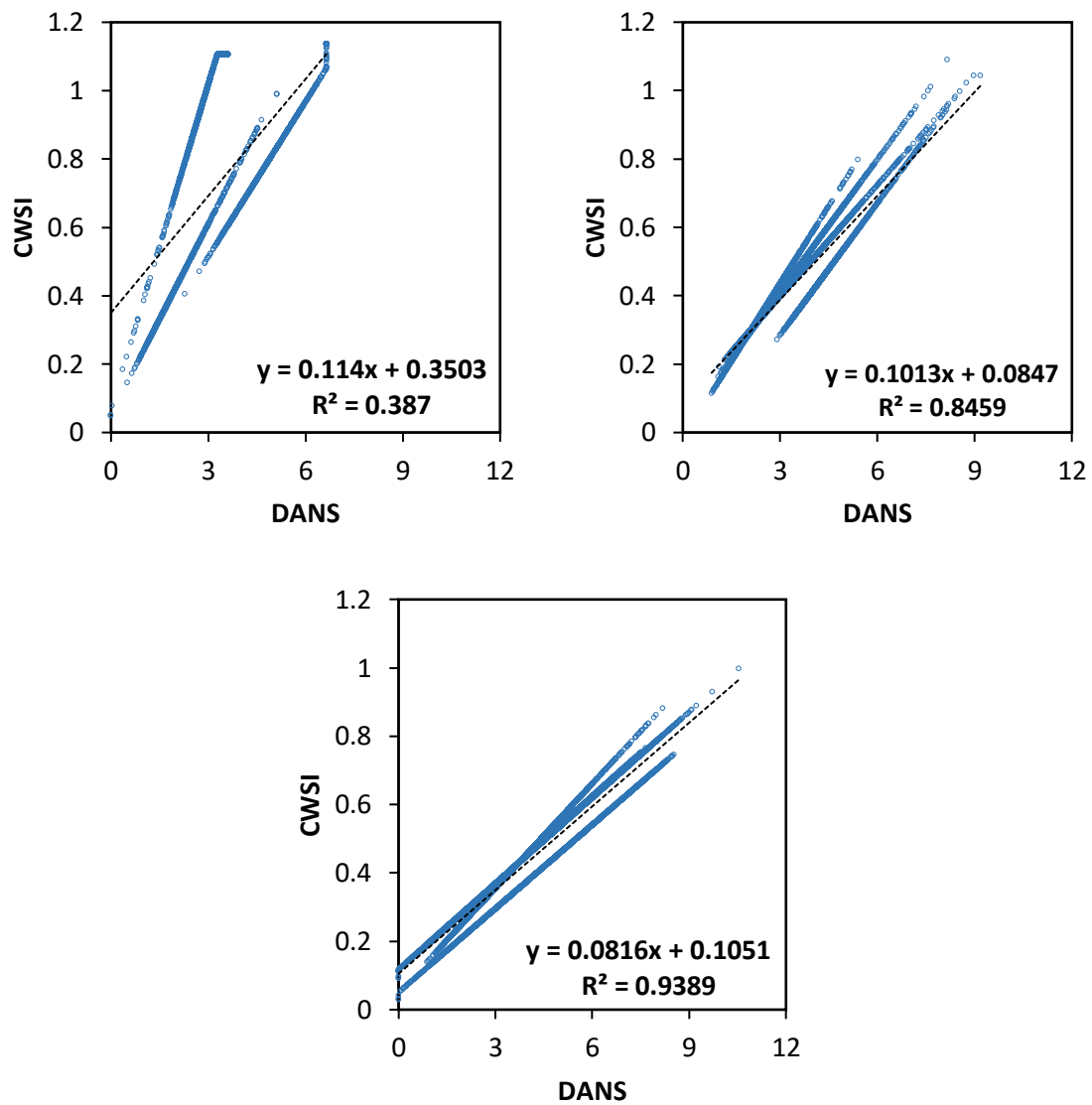
Figure 2. 13(a) Top-Left: Correlation value of 0.38 between CWSI and DANS for SCAL. (b) Top-Right: Correlation value of 0.84 between CWSI and DANS for ENREC1. (c) Bottom: Correlation value of 0.93 between CWSI and DANS for ENREC2.

The result after plotting all the measurements for each flight time together, showed each individual linear relationship with a positive linear correlation between the two values. As we see from the graphs that the determinant coefficients (R2) for SCAL, ENREC1, and ENREC2 are 0.38, 0.84, and 0.93, respectively. The difference in (R2) is due to the variation between the parameters (Twet and Tdry) of the functions being changed for each flight time. However, these scatterplots shows a strong relationship between these two variables, and DANS values can be estimated based on the equation with CWSI values.

2.3.4 CWSI Histogram Distribution-based Threshold Prediction Model

The objective of this research is to investigate if a different threshold CWSI is quantified during different times on a day in comparison to the hypothetical threshold CWSI usually quantified at or around solar noon. To trigger an irrigation event, estimating the threshold value and identifying crops with various stress levels is essential. Based on the statistical approach developed by Park et al., (2018), important evidence has been extracted out, from the generated CWSI maps.

A histogram distribution of CWSI values for each flight have been shown in Figures 2.14, 2.15, and 2.16 for ENREC1, ENREC2, and SCAL sites, respectively. Table 2.9 presents the summary statistics of mean, median and quartiles to calculate the threshold value for this study. The mean values from each flight have been computed and averaged. The mean CWSI values for each of the sites were 0.49, 0.51, and 0.49, respectively. Singh, et al. (2021), reported threshold CWSI value (0.5) for ENREC1. In addition, the water stress levels over a site have also been characterized in Table 2.8,

which is extracted as 25 and 75 quartiles are 0.3 and 0.6, respectively. Similar CWSI

levels are also reported in Singh, et al (2021) and DeJonge et al., (2015). As indicators of

whether the crop is experiencing stress.

Table 2. 6 CWSI Water stress levels based on 25 and 75 quantile range

CWSI	Water Stress Level
X < 0.3	Low Water Stress
0.3 - 0.6	Moderate Water Stress
X > 0.6	High Water Stress

Table 2. 7 Summary statistics extracted from CWSI Histogram Distribution for each flight to predict CWSI Threshold value (mean) and characterize water stress levels (Q1 – 25 quantile) (Q3 – 75 quantile)

Site	Date and Time	Min	Max	Mean	Q1	Q3
ENREC1	8/26/2020 11:25	0.015	1.043	0.499	0.377	0.603
	8/26/2020 14:20	0.085	1.086	0.5	0.36	0.6
	8/26/2020 16:32	-0.008	1.09	0.5	0.363	0.61
	8/26/2020 18:54	0.005	1.043	0.5	0.371	0.609
	Predictive Threshold			**0.499**	**0.36775**	**0.6055**
ENREC2	8/26/2020 10:37	0.131	1.04	0.5	0.351	0.627
	8/26/2020 13:30	0.09	1.036	0.567	0.393	0.723
	8/26/2020 15:45	0.027	1.031	0.5	0.347	0.638
	8/26/2020 18:03	0.108	1.048	0.49	0.353	0.612
	Predictive Threshold			**0.51**	**0.361**	**0.65**
SCAL	8/28/2020 11:00	0.029	1.105	0.5	0.367	0.605
	8/28/2020 13:30	0.01	1.136	0.5	0.354	0.627
	8/28/2020 16:00	0.002	0.989	0.49	0.359	0.637
	Predictive Threshold			**0.49**	**0.36**	**0.623**
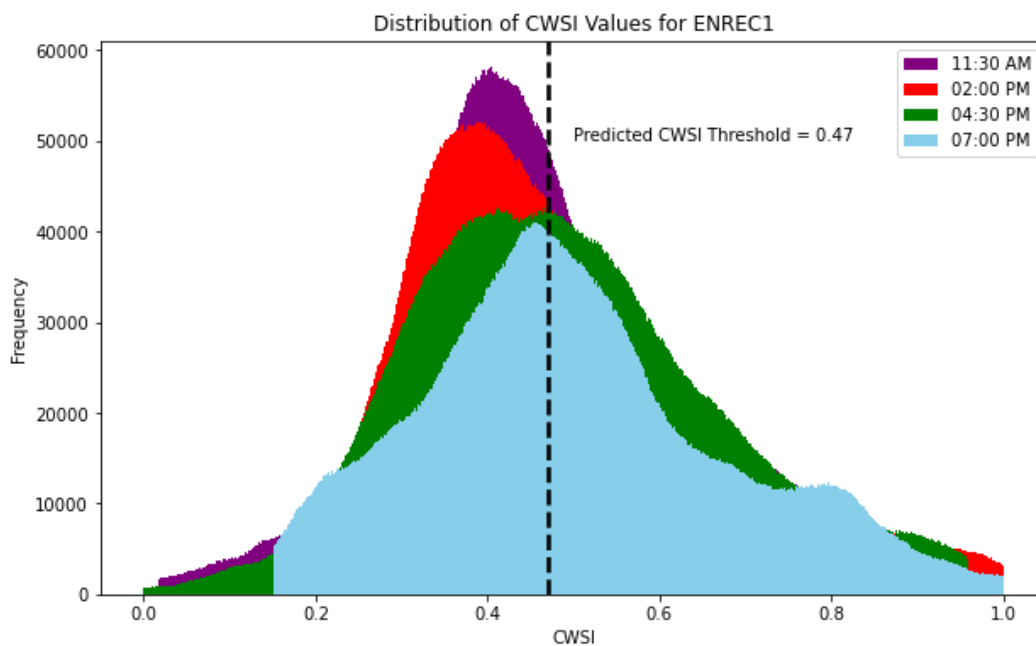
Figure 2. 14 CWSI histogram distribution created from CWSI maps of flights taken at 11:30 AM, 02:00PM, 04:30 PM, and 07:00 PM for site, ENREC1. Dotted line in between represents predicted CWSI Threshold value of 0.47 for 26th August, 2020.
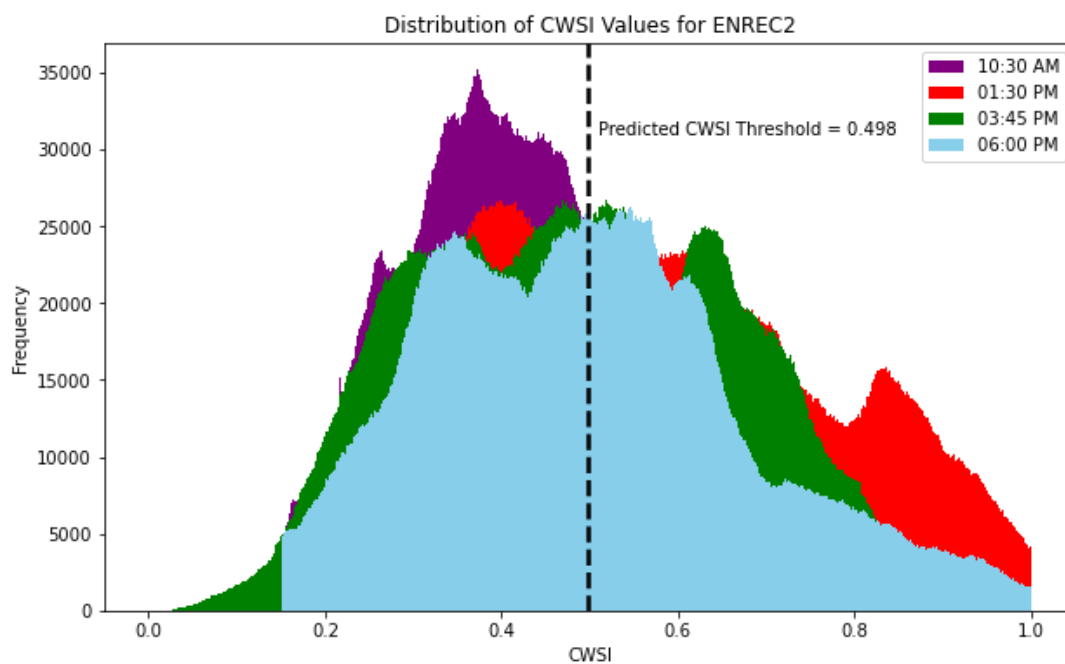
Figure 2. 15 CWSI histogram distribution created from CWSI maps of flights taken at 10:30 AM, 01:30PM, 03:45 PM, and 06:00 PM for site, ENREC2. Dotted line in between represents predicted CWSI Threshold value of 0.498 for 26th August, 2020.
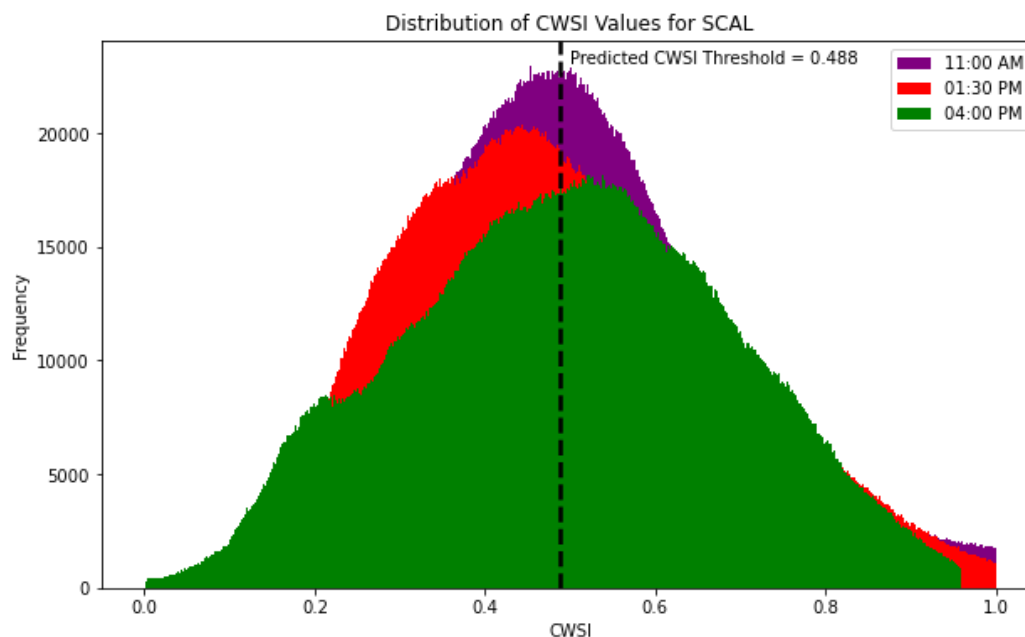
Figure 2. 16 CWSI histogram distribution created from CWSI maps of flights taken at 11:0 AM, 01:30PM, and 04:00 PM for site, SCAL. Dotted line in between represents predicted CWSI Threshold value of 0.488 for 28th August, 2020.

2.3.4 CWSI Sensitivity Analysis

The objective of CWSI calculation is to normalize the canopy temperatures is to reduce the influence of environment condition (e.g. air temperature, relative humidity, radiation), while maintaining sensitivity to plant water status. Previous researchers (Singh et al., 2021; O'Shaughnessy et al., 2017, 2012; DeJonge et al., 2015; Irmak et al., 2000;; Payero and Irmak, 2006; Peters and Evett, 2008; Taghvaeian et al., 2012) have studied and used empirical or theoretical approaches in determining CWSI sensitivity with respect to local environmental conditions. However, studies related to CWSI sensitivity with respect to the statistical approaches are minimal. This research is also intended to take into account on local meteorological factors and their influence on CWSI performance using the statistical approach. Four main important factor's (air temperature,

relative humidity, solar radiation and wind speed) that effecting CWSI values are examined below, for uniform irrigation treatment plots at the study research sites.

2.3.4.1 CWSI vs Air Temperature (T_{air})

A scatter plot between CWSI and T_{air} values, and line graph with respect to time, is shown in Figure 2.17(a-c), for ENREC1, ENREC2, and SSCAL field sites. Based on the scatter plot we observe that there is a strong positing correlation of 0.71, 0.81 and 0.98, respectively, between CWSI and T_{air} values. Generally, the increase in air temperature cause rapid evapotranspiration in plants i.e., to lose water rapidly, resulting in stress and an increase in canopy temperature. Thus, the relationship between the two variables are directly proportional. The line graph shows the mean value of CWSI and values of air temperature, both with respect to time. At morning, CWSI values are low, due to less air temperature. Whereas, during afternoon, air temperatures are at its maximum increasing CWSI values. Later in the evening CWSI values drops wit respect to drop in air temperature.

2.3.4.2 CWSI vs Relative Humidity (*RH*)

Figure 2.18 (a-c) shows the relationship of CWSI with respect to Relative. Humidity (RH). The scatter plot between these two variables shows a strong negative correlation of 0.86, 0.97, and 0.98, respectively. In general, the increase in surround air temperature causes the relative humidity to decrease and increase the vapor pressure deficit (VPD). Plants undergo the process of attaining equilibrium between the surrounding air moisture and canopy. When there is high VPD, it makes the plants harder to attain equilibrium conditions thereby increasing stress in plants. Thus, the relationship

between CWSI is inversely proportional to RH. The line graphs clearly indicate the

effects of RH decreased in afternoon due to increase in Tair and likewise increase in RH

during morning and evening times.

Figure 2. 17 (a) Top Left: Represents correlation between CWSI and Tair for ENREC1 (r2 = 0.71). (b) Middle Left: Represents correlation between CWSI and Tair for ENREC2 (r2 = 0.81). (c) Bottom Left: Represents correlation between CWSI and Tair for SCAL (r2 = 0.981). (d) Top Right: Represents correlation trend between CWSI and Tair for site: ENREC1 with respect to time of the day (e) Middle Right: Represents correlation trend between CWSI and Tair for site: ENREC2 with respect to time of the day. (f) Bottom Right: Represents correlation trend between CWSI and Tair for site: SCAL with respect to time of the day.
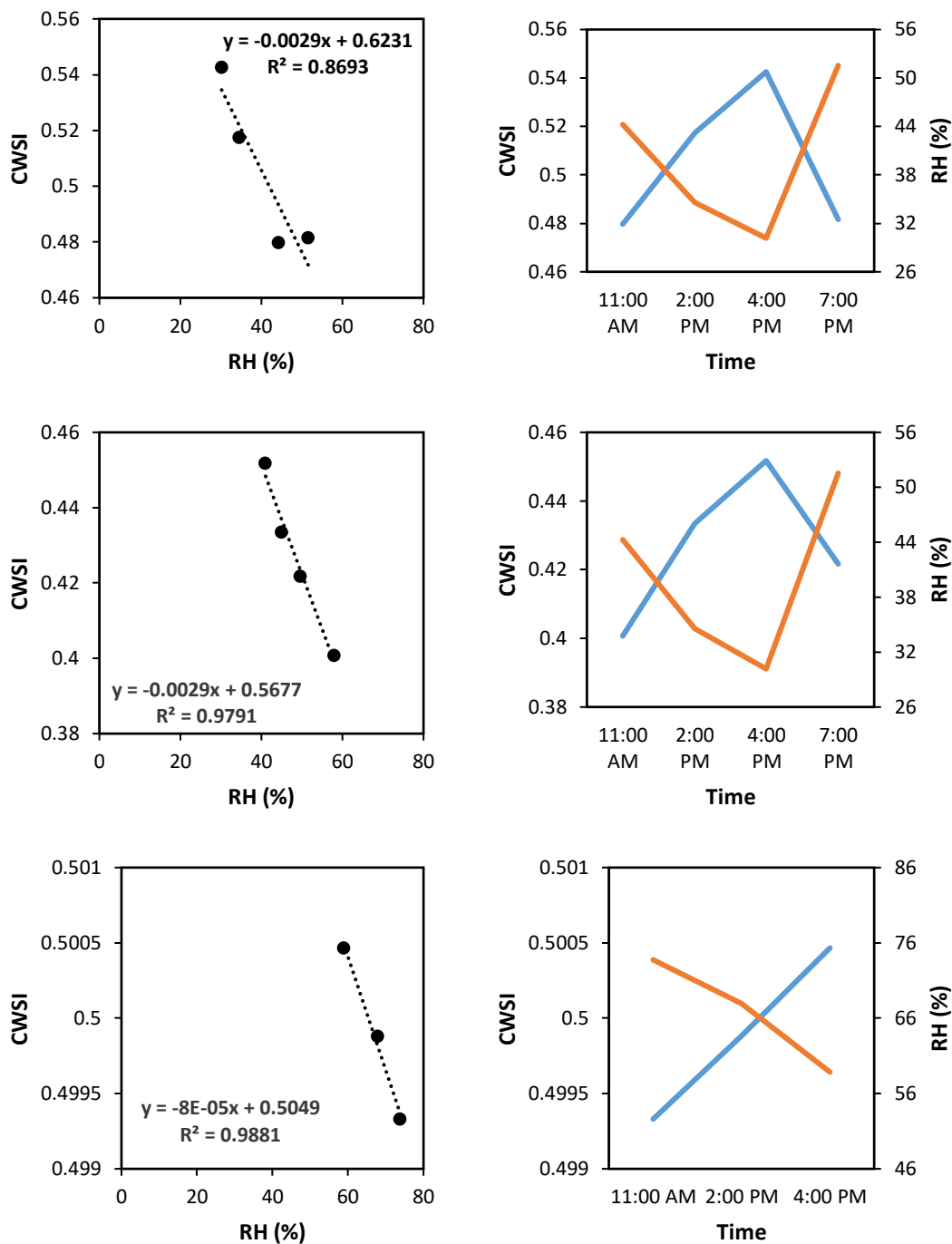
Figure 2. 18 (a) Top Left: Represents correlation between CWSI and Relative Humidity (RH) for ENREC1 (r2 = 0.86). (b) Middle Left: Represents correlation between CWSI and RH for ENREC2 (r2 = 0.97). (c) Bottom Left: Represents correlation between CWSI and RH for SCAL (r2 = 0.98). (d) Top Right: Represents correlation trend between CWSI and RH for site: ENREC1 with respect to time of the day (e) Middle Right: Represents correlation trend between CWSI and RH for site: ENREC2 with respect to time of the day. (f) Bottom Right: Represents correlation trend between CWSI and RH for site: SCAL with respect to time of the day.

2.3.4.3 CWSI vs Solar radiation (*SR*)

Solar radiation (SR) has a significant effect on CWSI values (Fig 2.19 (a-c)). The angle of the sun with respect to the crop canopy greatly determines the amount of solar radiation received. But these values on CWSI are largely influenced by the factors like cloud cover, wind, waterpower, air pollution, etc. From the scatter plot, we observed that there was weak positive relationship between CWSI and SR of 0.11, 0.16, and 0.01 respectively, indicating that the increase in SR values can increase the CWSI. But, as we see on the line graph, it clearly shows during later afternoon that in spite of having greater SR values, the CWSI value is decreased. This could be due other factors as mentioned above or plants having some cooling effect.

2.3.4.4 CWSI vs Wind Speed (*WS*)

The relationship between CWSI and windspeed (WS) is highly dependent on height of the instrument taken from nearby weather station. For the selected study sites, the nearby AWDN station has anemometers set up at 2 meters height. Since the chosen crop is soybean, the height usually less than the instrument height. During the windy conditions, the plants are subjected either hot air or cold air depending on surrounding temperature. Hot air increases the rate of transpiration from plants and can cause increase in stress rapidly. Thus, the relationship between the CWSI and WS for the selected study sites resulted in a weak positive correlation of 0.25, 0.32 and 0.96, respectively. The line graphs show a significant differences and is hard to explain the trends between these two variables.
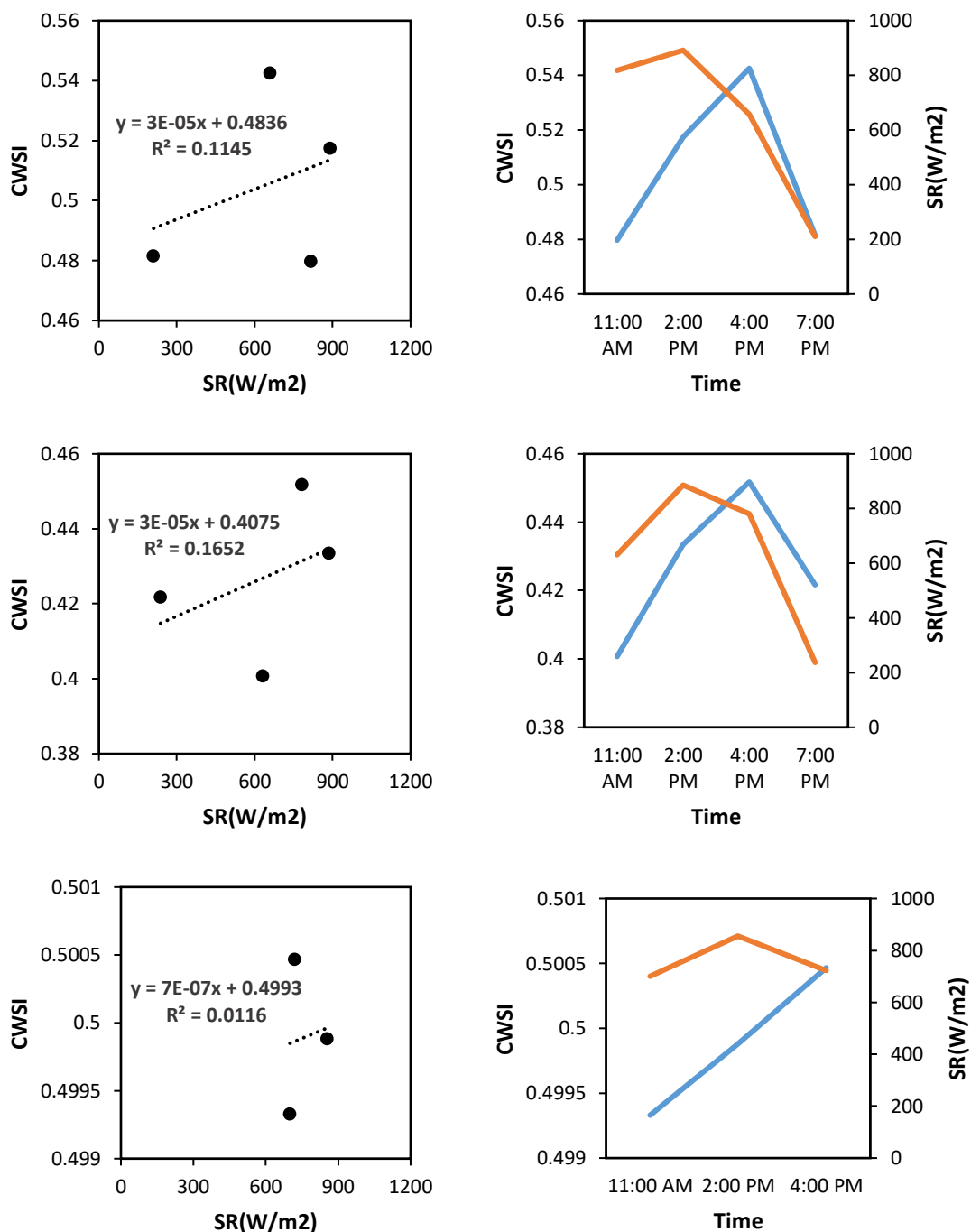
Figure 2. 19 (a) Top Left: Represents correlation between CWSI and Solar Radiation (SR) for ENREC1 (r2 = 0.11). (b) Middle Left: Represents correlation between CWSI and SR for ENREC2 (r2 = 0.16). (c) Bottom Left: Represents correlation between CWSI and SR for SCAL (r2 = 0.011). (d) Top Right: Represents correlation trend between CWSI and SR for site: ENREC1 with respect to time of the day (e) Middle Right: Represents correlation trend between CWSI and SR for site: ENREC2 with respect to time of the day. (f) Bottom Right: Represents correlation trend between CWSI and SR for site: SCAL with respect to time of the day.
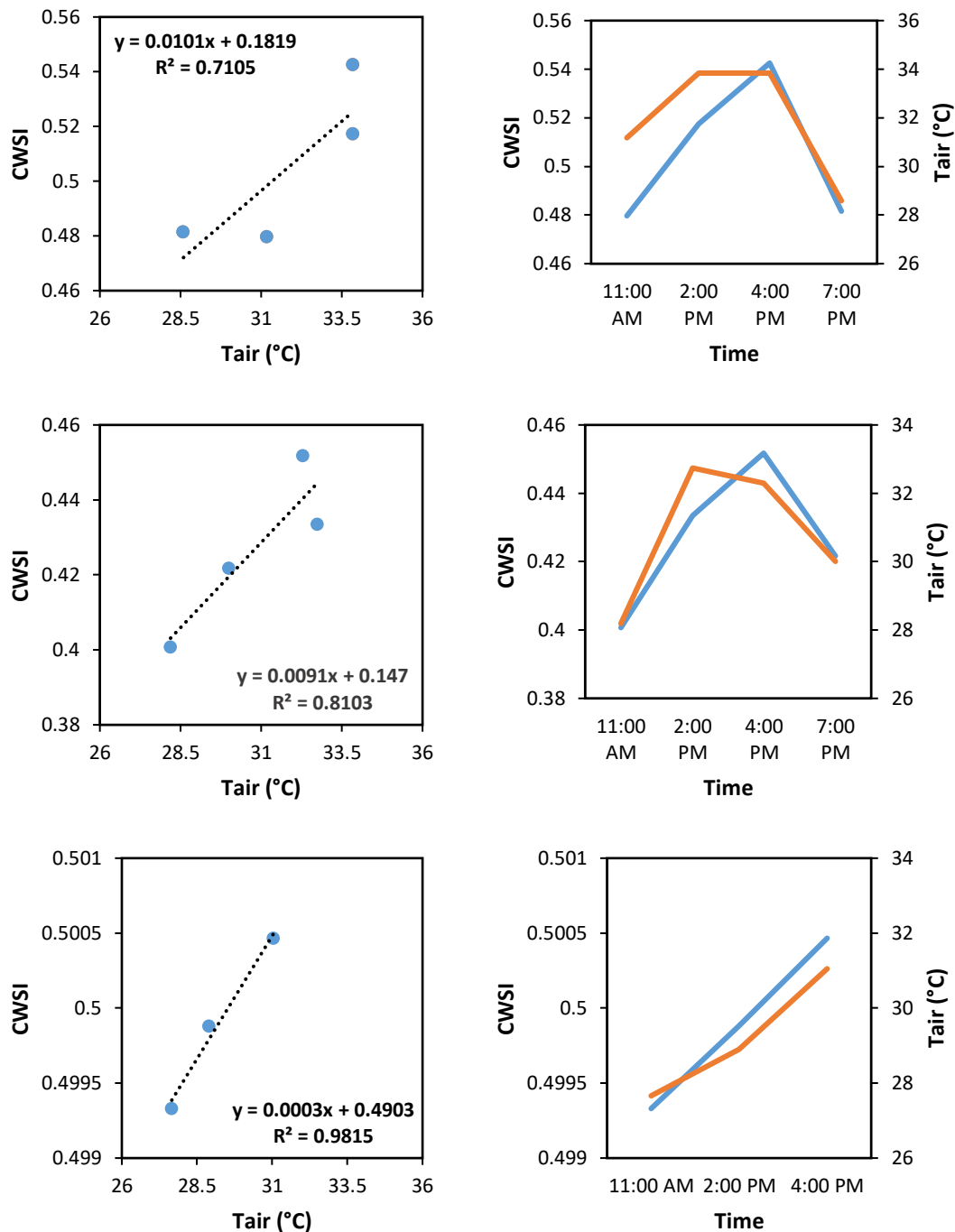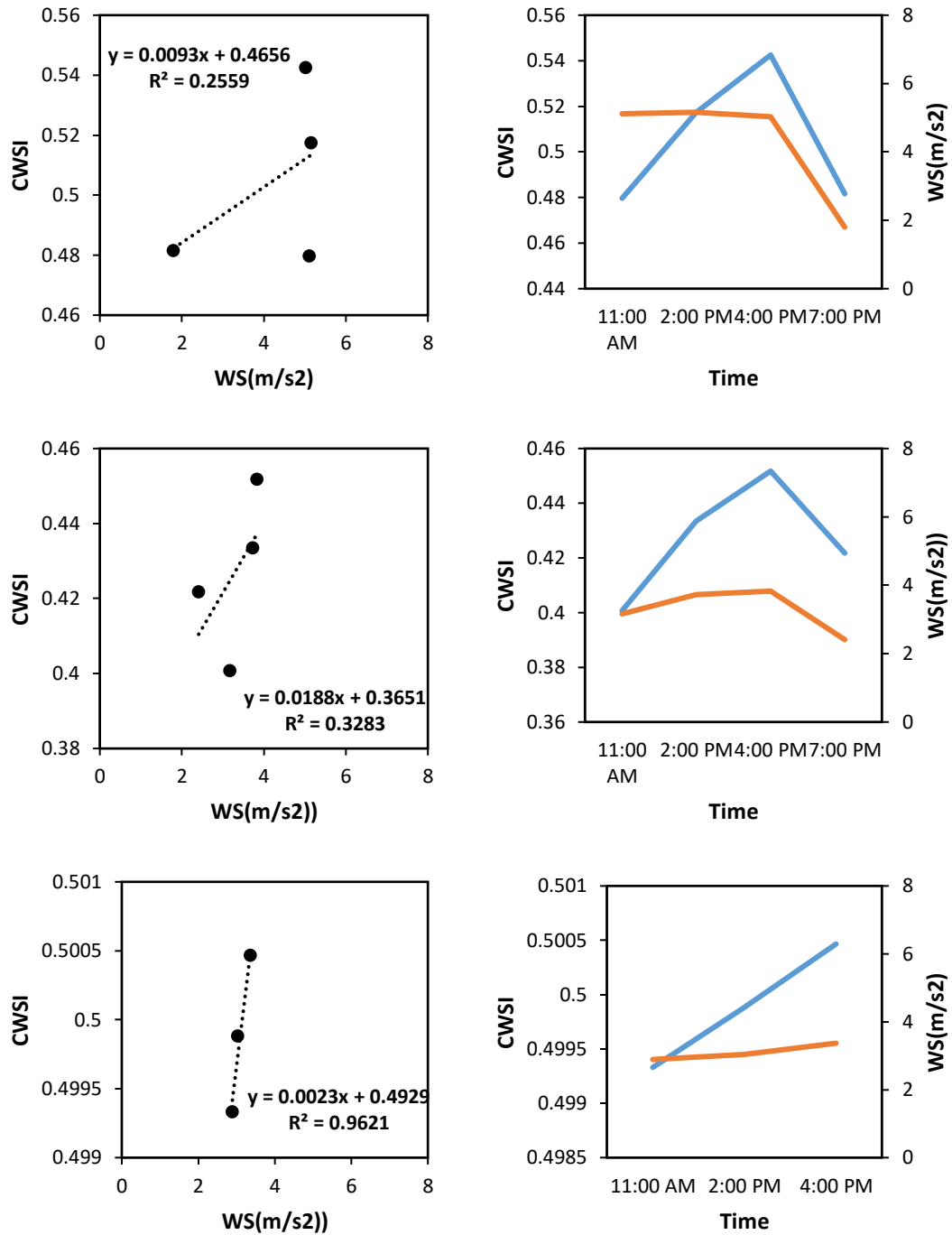
Figure 2. 20 (a) Top Left: Represents correlation between CWSI and Wind Speed (WS) for ENREC1 (r2 = 0.25). (b) Middle Left: Represents correlation between CWSI and WS for ENREC2 (r2 = 0.32). (c) Bottom Left: Represents correlation between CWSI and WS for SCAL (r2 = 0.096). (d) Top Right: Represents correlation trend between CWSI and WS for site: ENREC1 with respect to time of the day (e) Middle Right: Represents correlation trend between CWSI and WS for site: ENREC2 with respect to time of the day. (f) Bottom Right: Represents correlation trend between CWSI and WS for site: SCAL with respect to time of the day.

2.4 Discussion

The objective of this study was to observe discrepancies between CWSI values at different times of the day considering that they are hypothetically assumed to be taken at or near solar noon. To quantify this objective high-resolution thermal and multispectral images were captured using an unmanned aerial system (UAS) on three different research sites in Eastern Nebraska. The estimation of water stress indices for these high frequency flights are computed using the statistical approach developed by Park et al., 2018, for this research. The reason for considering statistical approach over empirical and theoretical approach is due to reduced requirements of parameters that are required in estimating the CWI and DANS values, and increasing the automation time of generating these water stress maps. The only requirements for this approach is the use of thermal imagery captured from UAS, and nearby local meteorological data, as an input for thermal calibration model (Maguire, 2021) and CWSI sensitivity analysis. The whole research was carried out based on an assumption that there is an extensive range of water stress levels during a moisture stress period over the field, involving various irrigation treatments.

The first objective of this research is to identify and characterize the temporal nature of spatial canopy stress patters for the soybean crop. This was achieved through the creation of CWSI, DANS and VI maps, that visually depict the differences in canopy stress patterns for selected three different research sites in Eastern Nebraska. Moreover, statistical tables to determine the thresholds of Twet and Tdry values analyzed to distribution of canopy temperatures. The lower and upper threshold values, i.e. Twet and

Tdry was extracted by eliminating the soil and mixed canopy-soil pixels with each TIR imagery and a Gaussian mixture model (GMM) is fitted to the temperature distribution histogram for calculation of water stress indices. In addition to the development of water stress maps, difference between canopy and air temperature (ΔT) is also analyzed to understand the spatial variability and crop stress pattern. Based on the descriptive statistical table computing ΔT, the interquartile range for rainfed and uniform treatments was extracted for ENREC1 and ENREC2 sites, that can also be used as a threshold value to apply irrigation. Finally, correlation plots between CWSI and DANS are also created to understand the relationship between the two variables as an indication of plant stress.

Coming to the second objective, this research developed a new CWSI histogram-based threshold prediction method and also characterized the water stress levels into low, moderate and high using quantiles extracted from histogram distribution. Descriptive statistics and figures displayed in the above results sections shows mean and quantile range values of CWSI taken for each flight. This average value of mean represents the threshold value of CWSI and the 25 and 75 quantile values represent the cut-off between low water stress and high water stress crops.

The third objective of this research is to perform a sensitivity analysis between CWSI and common meteorological factors namely air temperature, relative humidity, wind speed and solar radiation using statistical CWSI approach. From the literature review, it was well known that the pervious researcher has always accounted for meteorological effects based on theoretical or empirical equations used. However, minimal or no study was conducted using statistical approach. In view of the parameters

of the crop canopy examined, the study discovered that air temperature, solar radiation, wind speed were positively correlated to CWSI level except relative humidity, being negatively correlated. Indeed, increased levels of air temperature, solar radiation, and wind speed caused the plants to experience more water stress levels. This was mostly experienced in the morning until afternoon hours when the rate of transpiration in plants was quite high. Later in evening, CWSI values dropped with respect to decrease in air temperature and solar radiation principally.

2.5 Limitations

This research was conducted during full canopy growth stage which is crucial period for soybean crop. Due to various reasons addressed in Chapter 3, the research did not explore for water stress patters over different growth stages. In addition, the accuracy of canopy temperatures extracted from UAV thermal imagery can be affected by various parameters. However, with the help of comprehensive study conducted by Maguire, 2021 for improving the accuracy of thermal images has potentially mitigated the effects of environmental factors like altitude, air temperature, relative humidity and atmospheric pressure subjected to the time of UAV flight. One more advantage of Magui, 2021 method is that the thermal calibrated image using linear regression model has taken into account of using reference infrared thermometers (IRTs) stationed at ENREC1 to train the model for obtaining the temperature values close to IRT canopy temperature. Results of calibration model is show in above methods.

It is also well noted that this research has some possible limitations of the implied statistical CWSI approach for developing water stress maps and identifying threshold

value based on histogram distribution, for all possible conditions in the field. Park et al., 2018 has clearly mentioned in his study that the estimated T_{dry} from GMM distribution should be less that the that of T_{air}, else, it can indicate non-severe crop water stress. In contrast, if the canopy temperature distribution range is very narrow and close to the T_{dry} prediction by Tair, most crops are water-stressed. Nevertheless, it is necessary to continue future research experiments in order to evaluate this approach at any phonological crop growth stages.

2.6 Conclusion

Use of UAV technology equipped with various sensors has become common in present research studies to identify crop water stress needs spatially and effectively. Through the examination of standardized CWSI values through a statistical approach, it was revealed how CWSI was sensitive to environmental conditions. Factors like air temperature, solar radiation, wind speed were positively correlated to crop water stress index level except relative humidity. Moreover, it was revealed from the correlation plots and histogram distribution that the CWSI had a consistency for statistical CWSI approach in its range from late morning till late afternoon window, creating possibility for collection and estimating of CWSI at any time of the day, mainly at sunshine hours. However, more research is needed to ensure that all factors associated with estimation of crop stress are put into perspective. As a future work, further research on different crop fields and different crop phonological stages needs to be examined to make the present method applicable to general cases.

2.7 References

Alchanatis, V., Cohen, Y., Cohen, S., Moller, M., Sprinstin, M., Meron, M., Tsipris, J., Saranga, Y. and Sela, E. (2010) Evaluation of different approaches for estimating and mapping crop water status in cotton with thermal imaging. Precision Agriculture, 11.

Barker, J.B., Heeren, D.M., Daugherty, R.B., Neale, C.M.U., Rudnick, D.R., 2018. Evaluation of variable rate irrigation using a remote-sensing-based model. Agric. Water Manag. 203, 63–74. https://doi.org/10.1016/j.agwat.2018.02.022.

Barsi, J.A., Barker, J. L., & Schott, J. R. (2003). An Atmospheric Correction Parameter Calculator for a single thermal band earth-sensing instrument. IGARSS 2003. 2003 IEEE International Geoscience and Remote Sensing Symposium. Proceedings (IEEE Cat. No.03CH37477), 5, 3014–3016. doi.org/10.1109/IGARSS.2003.1294665

Bellvert, J., Zarco-Tejada, P., Girona, J. and Fereres, E. (2014) Mapping crop water stress index in a 'Pinot-noir' vineyard: comparing ground measurements with thermal remote sensing imagery from an unmanned aerial vehicle. Precision Agriculture, 15, 361-376.

Berni, J. A. J., Zarco-Tejada, P. J., Sepulcre-Cantó, G., Fereres, E. and Villalobos, F. (2009b) Mapping canopy conductance and CWSI in olive orchards using high resolution thermal remote sensing imagery. Remote sens. environ., 113, 2380-2388.

Bhatti, S., D. M. Heeren, S. A. O'Shaughnessy, S. R. Evett, M. S. Maguire, S. P.

Kashyap, and C. M. U. Neale. 2021. Comparison of stationary and mobile canopy sensing systems for irrigation management of maize and soybean in Nebraska. Applied Engineering in Agriculture (in review).

Bhatti, S., Heeren, D.M., Barker, J.B., Neale, C.M.U., Woldt, W.E., Maguire, M.S., Rudnick, D.R., 2020. Site-specific irrigation management in a sub-humid climate using a spatial evapotranspiration model with satellite and airborne imagery. Agric. Water Manag. 230, 1–13. https://doi.org/10.1016/j.agwat.2019.105950.

Bhusal, N., Bhusal, S. J., & Yoon, T. M. (2018). Comparisons of physiological and anatomical characteristics between two cultivars in bi-leader apple trees (Malus× domestica Borkh.). *Scientia Horticulturae*, *231*, 73-81. https://www.sciencedirect.com/science/article/pii/S0304423817307197

Bian, J., Zhang, Z., Chen, J., Chen, H., Cui, C., Li, X., ... & Fu, Q. (2019). Simplified evaluation of cotton water stress using high resolution unmanned aerial vehicle thermal imagery. Remote Sensing, 11(3), 267.

Blaya-Ros, P. J., Blanco, V., Domingo, R., Soto-Valles, F., & Torres-Sánchez, R. (2020). Feasibility of low-cost thermal imaging for monitoring water stress in young and mature sweet cherry trees. *Applied Sciences*, *10*(16), 5461. https://www.mdpi.com/791424

Brunsell, N. A., & Gillies, R. R. (2002). Incorporating surface emissivity into a thermal atmospheric correction. Photogrammetric Engineering and Remote Sensing, 68(12), 1263-1269.

Candogan, B. N., Sincik, M., Buyukcangaz, H., Demirtas, C., Goksoy, A. T., & Yazgan, S. (2013). Yield, quality and crop water stress index relationships for deficit-irrigated soybean [Glycine max (L.) Merr.] in sub-humid climatic conditions. *Agricultural Water Management*, *118*, 113-121.

Chen, X., Yang, D., Chen, J., & Cao, X. (2015). An improved automated land cover updating approach by integrating with downscaled NDVI time series data. *Remote sensing letters*, *6*(1), 29-38.

Cohen, Y., Alchanatis, V., Meron, M., Saranga, Y. and Tsipris, J. (2005) Estimation of leaf water potential by thermal imagery and spatial analysis. J. Exp. Bot., 56, 1843-1852.

Colaizzi, P. D., O'Shaughnessy, S. A., Evett, S. R., & Howell, T. A. (2012). Using plant canopy temperature to improve irrigated crop management.

Crusiol, L. G. T., Nanni, M. R., Furlanetto, R. H., Sibaldelli, R. N. R., Cezar, E., Mertz-Henning, L. M., ... & Farias, J. R. B. (2020). UAV-based thermal imaging in the assessment of water status of soybean plants. *International Journal of Remote Sensing*, *41*(9), 3243-3265. https://www.tandfonline.com/doi/abs/10.1080/01431161.2019.1673914?

Crusiol, L. G. T., Nanni, M. R., Furlanetto, R. H., Sibaldelli, R. N. R., Cezar, E., Sun, L., ... & Farias, J. R. B. (2021). Yield Prediction in Soybean Crop Grown under Different Levels of Water Availability Using Reflectance Spectroscopy and Partial Least Squares Regression. Remote Sensing, 13(5), 977.

DeJonge, K. C., Taghvaeian, S., Trout, T. J., & Comas, L. H. (2015). Comparison of canopy temperature-based water stress indices for maize. Agricultural water management, 156, 51-62.

Döpper, V., Gränzig, T., Kleinschmit, B., & Förster, M. (2020). Challenges in UAS-based TIR imagery processing: image alignment and uncertainty quantification. *Remote Sensing*, *12*(10), 1552.

Emekli, Y., Bastug, R., Buyuktas, D., & Emekli, N. Y. (2007). Evaluation of a crop water stress index for irrigation scheduling of bermudagrass. Agricultural water management, 90(3), 205-212.

Fernández, J. E. (2017). Plant-based methods for irrigation scheduling of woody crops. *Horticulturae*, *3*(2), 35. https://www.mdpi.com/200528 https://www.mdpi.com/200528

Fuentes, S., Bei, R., Pech, J. and Tyerman, S. (2012) Computational water stress indices obtained from thermal image analysis of grapevine canopies. Irrig. Sci., 30, 523-536.

Gates, David M. 1964. "Leaf Temperature and Transpiration." Agronomy Journal 56(3): 273–77 .

Idso, S. B., Jackson, R. D., Pinter, J. P. J., Reginato, R. J. and Hatfield, J. L. (1981) Normalizing the stress-degree-day parameter for environmental variability. Agric. Meteorol., 24, 45-55.

Ihuoma, S. O., & Madramootoo, C. A. (2017). Recent advances in crop water stress detection. *Computers and Electronics in Agriculture*, *141*, 267-275.

Irmak, S., Haman, D. Z., & Bastug, R. (2000). Determination of crop water stress index for irrigation timing and yield estimation of corn. Agronomy Journal, 92(6), 1221-1227.

Jackson, R. D., Idso, S. B., Reginato, R. J. and Pinter, P. J., Jr. (1981) Canopy temperature as a crop water stress indicator Wheat. Water Resources Research, 17, 1133-1138.

Jackson, R. D., Reginato, R. J. and Idso, S. B. (1977) Wheat canopy temperature: a practical tool for evaluating water requirements. Water Resources Research (USA), 13, 651.

Leinonen, I. and Jones, H. G. (2004) Combining thermal and visible imagery for estimating canopy temperature and identifying plant stress. J. Exp. Bot., 55, 1423-1431.

López-López, R., Ramírez, R. A., Sánchez-Cohen, I., Bustamante, W. O. and GonzálezLauck, V. (2011) Evapotranspiration and Crop Water Stress Index in Mexican Husk Tomatoes (Physalis ixocarpa Brot). In Evapotranspiration-From Measurements to Agricultural and Environmental Applications InTech, Jiutepec, México.

Maguire, M. S. (2018). An evaluation of unmanned aerial system multispectral and thermal infrared data as information for agricultural crop and irrigation management (Doctoral dissertation, University of Nebraska-Lincoln).

Maguire, M. S., Neale, C. M., & Woldt, W. E. (2021). Improving Accuracy of Unmanned Aerial System Thermal Infrared Remote Sensing for Use in Energy Balance

Models in Agriculture Applications. Remote Sensing, 13(9), 1635.

Martínez, J., Egea, G., Agüera, J., & Pérez-Ruiz, M. (2017). A cost-effective canopy temperature measurement system for precision agriculture: a case study on sugar beet. *Precision Agriculture*, *18*(1), 95-110. https://link.springer.com/content/pdf/10.1007/s11119-016-9470-

Martínez, J., Egea, G., Agüera, J., & Pérez-Ruiz, M. (2017). A cost-effective canopy temperature measurement system for precision agriculture: a case study on sugar beet. Precision Agriculture, 18(1), 95-110.

Meron, M., Sprintsin, M., Tsipris, J., Alchanatis, V. and Cohen, Y. (2013) Foliage temperature extraction from thermal imagery for crop water stress determination. Precision Agriculture, 14, 467-477.

Meron, M., Tsipris, J., Orlov, V., Alchanatis, V. and Cohen, Y. (2010a) Crop water stress mapping for site-specific irrigation by thermal imagery and artificial reference surfaces. Precision Agriculture, 11, 148-162.

Meron, M., Tsipris, J., Orlov, V., Alchanatis, V. and Cohen, Y. (2010b) Crop water stress mapping for site-specific irrigation by thermal imagery and artificial reference surfaces. Precision Agriculture, 11, 148-162.

Meron, M., Tsipris, J., Orlov, V., Alchanatis, V. and Cohen, Y. (2010a) Crop water stress mapping for site-specific irrigation by thermal imagery and artificial reference surfaces. Precision Agriculture, 11, 148-162.

Meron, M., Tsipris, J., Orlov, V., Alchanatis, V. and Cohen, Y. (2010b) Crop water stress mapping for site-specific irrigation by thermal imagery and artificial reference surfaces. Precision Agriculture, 11, 148-162.

Nielsen, D. C. (1990). Scheduling irrigations for soybeans with the crop water stress index (CWSI). Field Crops Research, 23(2), 103-116.

O'Shaughnessy, S. A., Andrade, M. A., & Evett, S. R. (2017). Using an integrated crop water stress index for irrigation scheduling of two corn hybrids in a semi-arid region. Irrigation Science, 35(5), 451-467.

O'Shaughnessy, S. A., Evett, S. R., Colaizzi, P. D., & Howell, T. A. (2012). A crop water stress index and time threshold for automatic irrigation scheduling of grain sorghum. Agricultural water management, 107, 122-132.

O'Shaughnessy, S. A., Evett, S. R., Colaizzi, P. D., & Howell, T. A. (2012). A crop water stress index and time threshold for automatic irrigation scheduling of grain sorghum. Agricultural water management, 107, 122-132.

Park, S. (2018). Estimating plant water stress and evapotranspiration using very-high-resolution (VHR) UAV imagery (Doctoral dissertation).

Park, S., Nolan, A., Ryu, D., Fuentes, S., Hernandez, E., Chung, H., & O'connell, M. (2015, November). Estimation of crop water stress in a nectarine orchard using high-resolution imagery from unmanned aerial vehicle (UAV). In Proceedings of the 21st International Congress on Modelling and Simulation, Gold Coast, Australia (Vol. 29).

Park, S., Ryu, D., Fuentes, S., Chung, H., Hernández-Montes, E., & O'Connell, M. (2017). Adaptive estimation of crop water stress in nectarine and peach orchards using high-resolution imagery from an unmanned aerial vehicle (UAV). *Remote Sensing*, *9*(8), 828. https://www.mdpi.com/215938

Park, S., Ryu, D., Fuentes, S., Chung, H., Hernández-Montes, E., & O'Connell, M. (2017). Adaptive estimation of crop water stress in nectarine and peach orchards using high-resolution imagery from an unmanned aerial vehicle (UAV). Remote Sensing, 9(8), 828.

Payero, J. O., & Irmak, S. (2006). Variable upper and lower crop water stress index baselines for corn and soybean. Irrigation Science, 25(1), 21-32.

Peters, R.T., Evett, S.R., 2008. Automation of a center pivot using the temperature-timethreshold method of irrigation scheduling. J. Irrig. Drain. Eng. 134 (3), 286–291. https://doi.org/10.1061/ASCE_0733-9437(2008)_134:3(286).

Poblete, T., Ortega-Farías, S., & Ryu, D. (2018). Automatic coregistration algorithm to remove canopy shaded pixels in UAV-borne thermal images to improve crop water stress; index estimation of a drip-irrigated Cabernet Sauvignon vineyard. *Sensors*, *18*(2), 397. https://www.mdpi.com/258744

Poblete-Echeverría, C., Espinace, D., Sepúlveda-Reyes, D., Zúñiga, M., & Sanchez, M. (2017, June). Analysis of crop water stress index (CWSI) for estimating stem water potential in grapevines: Comparison between natural reference and baseline approaches. In *VIII International Symposium on Irrigation of Horticultural Crops 1150* (pp. 189-194). https://www.actahort.org/books/1150/1150_27.htm

Poblete-Echeverría, C., Sepulveda-Reyes, D., Ortega-Farias, S., Zuñiga, M. and Fuentes, S. (2016) Plant water stress detection based on aerial and terrestrial infrared thermography: a study case from vineyard and olive orchard. In Acta horticulturae Brisbane, Australia, pp. 141-146.

Rud, R., Cohen, Y., Alchanatis, V., Levi, A., Brikman, R., Shenderey, C., Heuer, B., Markovitch, T., Dar, Z., Rosen, C., Mulla, D. and Nigon, T. (2014) Crop water stress index derived from multi-year ground and aerial thermal images as an indicator of potato water status. Precision Agriculture, 15, 273-289.

Santesteban, L. G., Di Gennaro, S. F., Herrero-Langreo, A., Miranda, C., Royo, J. B., & Matese, A. (2017). High-resolution UAV-based thermal imaging to estimate the instantaneous and seasonal variability of plant water status within a vineyard. *Agricultural Water Management*, *183*, 49-59. https://www.sciencedirect.com/science/article/pii/S0378377416303201

Santesteban, L. G., Di Gennaro, S. F., Herrero-Langreo, A., Miranda, C., Royo, J. B., & Matese, A. (2017). High-resolution UAV-based thermal imaging to estimate the instantaneous and seasonal variability of plant water status within a vineyard. Agricultural Water Management, 183, 49-59.

Singh, J., Ge, Y., Heeren, D. M., Walter-Shea, E., Neale, C. M., Irmak, S., ... & Maguire, M. S. (2021). Inter-relationships between water depletion and temperature differential in row crop canopies in a sub-humid climate. *Agricultural Water Management*, *256*, 107061.

Singh, J., Heeren, D. M., Ge, Y., Bai, G., Neale, C. M., Maguire, M. S., & Bhatti, S. (2021). Sensor-based irrigation of maize and soybean in East-Central Nebraska under a sub-humid climate. In *2021 ASABE Annual International Virtual Meeting* (p. 1). American Society of Agricultural and Biological Engineers.

Singh, J., Heeren, D. M., Ge, Y., Bai, G., Neale, C. M., Maguire, M. S., & Bhatti, S. (2021). Sensor-based irrigation of maize and soybean in East-Central Nebraska under a sub-humid climate. In 2021 ASABE Annual International Virtual Meeting (p. 1). American Society of Agricultural and Biological Engineers.

Sharma, V., & Irmak, S. (2021). Comparative analyses of variable and fixed rate irrigation and nitrogen management for maize in different soil types: Part I. Impact on soil-water dynamics and crop evapotranspiration. Agricultural Water Management, 245, 106644.

Taghvaeian, S., Chavez, ´ J.L., Hansen, N.C., 2012. Infrared thermometry to estimate crop water stress index and water use of irrigated maize in northeastern colorado. Remote Sens. 4, 3619–3637. https://doi.org/10.3390/rs4113619.

Taghvaeian, S., Comas, L., DeJonge, K.C., Trout, T.J., 2014. Conventional and simplified canopy temperature indices predict water stress in sunflower. Agric. Water Manag. 144, 69–80. https://doi.org/10.1016/j.agwat.2014.06.003.

Tanner C B (1963). Plant temperatures. Agronomy Journal 55, 210-211

Thenmozhi, K., & Reddy, U. S. (2017, November). Image processing techniques for insect shape detection in field crops. In *2017 International Conference on Inventive Computing and Informatics (ICICI)* (pp. 699-704). IEEE.

Yao, H., Qin, R., & Chen, X. (2019). Unmanned aerial vehicle for remote sensing

    applications—A review. *Remote Sensing*, *11*(12), 1443.

    https://www.mdpi.com/481544

Yazar, A., Howell, T. A., Dusek, D. A., & Copeland, K. S. (1999). Evaluation of crop

    water stress index for LEPA irrigated corn. Irrigation Science, 18(4), 171-180.

Zarco-Tejada, P. J., González-Dugo, V. and Berni, J. A. J. (2012) Fluorescence,

    temperature and narrow-band indices acquired from a UAV platform for water

    stress detection using a micro-hyperspectral imager and a thermal camera.

    Remote sens. environ., 117, 322-337.

Zhang, L., Niu, Y., Zhang, H., Han, W., Li, G., Tang, J., & Peng, X. (2019). Maize

    canopy temperature extracted from UAV thermal and RGB imagery and its

    application in water stress monitoring. *Frontiers in plant science*, *10*, 1270.

    https://www.frontiersin.org/articles/10.3389/fpls.2019.01270/fullP

Zhang, L., Zhang, H., Niu, Y., & Han, W. (2019). Mapping maize water stress based on

    UAV multispectral remote sensing. Remote Sensing, 11(6), 605.

CHAPTER 3. CHALLENGES INVOLVED IN CONDUCTING HIGH-FREQUENCY UAV FLIGHTS FOR ESTIMATION OF PLANT WATER STRESS

In this chapter, we will discuss the key challenges encountered during the development of plant water stress maps for this research, starting from data collection to processing issues. This can also serve as a useful guide for improving further research methodologies using unmanned aerial systems (UAVs) for agricultural operations.

3.1 Conducting High-Frequency UAV Flights

3.1.1 Pre-flight Planning

In order to operate or conduct research involving unmanned aerial vehicles, researchers are required to obtain an FAA Part 107 remote pilot license following all rules and regulations outlined by the Federal Aviation Administration (FAA). For safety reasons, a researcher must ensure that the UAV being used is registered with the FAA and that a copy of the registration with the FAA number is always attached to the drone. An insurance policy is also necessary in the event of any accidental damage caused during research operations.

For this research, an FAA registered DJI Matrice M600 was used, which was permitted to fly at the University of Nebraska-Lincoln's research locations. In advance of the flight operations, an in-depth investigation was conducted on the selected research sites (ENREC1, ENREC2 and SCAL) to identify potential obstacles, such as trees, power lines, birds, and insects, in order to minimize damage and enhance the likelihood of successful data collection.

The research was carried out using UgCS Drone Mission Planning and Flight Control (UgCS, USA) software for survey and planning the flight missions. The software allows users to create flight routes with customized flight speed, altitude, orientation, and side spacing, front and side overlap settings are all pre-programmed requiring less human interaction during actual flight.

Drone safety and pre-flight checklist recommended by manufacturer has always been followed during this entire data collection period. A safety tool kit and extra parts were always carried on board to fix quick issues during long research flights. Drone inspection and maintenance was carried out each day before setting out to the field.

3.1.2 Weather and Local Environmental Considerations

This research is highly dependent upon weather and environmental conditions since the UAV was used on multiple occasions during the day for high-frequency data collection. Prior to the flights, hourly weather data from National Weather Service Forecast Office (https://forecast.weather.gov/), and cloud movement monitoring from NOAA Geostationary satellite server (https://www.goes.noaa.gov/), was used for planning of flight missions.

Initially, the goal of the original research was to conduct six UAV flights approximately every day, starting from the day after an irrigation event until the day before another irrigation event, to monitor and study the crop stress pattern and recovery. However, it was not possible to achieve this objective because changing cloud cover and wind profiles made it impossible to capture data continuously within a day. The maximum number of flights could be obtained on a sunny clear day with low wind

profile was five. Please see the appendix section for a complete list of UAV flight campaigns conducted for this research. The total number of flights conducted were 47.

In order to keep the drone safe at all times in field, an enclosed university vehicle was utilized regardless of changing weather local environmental conditions.

3.1.3 Batteries and Charging Issues

Predicting the number of battery sets required and charging issues are another major obstacle to successful data capture. With the DJI Matrice M600, the maximum flight time at full payload capacity is expected to be around 16 minutes. The total amount of batteries available was three sets. On average, each research field required 15-17 minutes to fly, plus additional 3 minutes for warming up and connecting the drone to an iPad. Due to a shorter UAV flight time, two batteries were used per research field for one time data collection. In order to conduct multiple flights in a day, the batteries were charged periodically from the nearby center pivot control outlet at ENREC1 and ENREC2, and nearby farm shop at SCAL. An additional backup was provided by a car power battery charger. Approximately 90 to 110 minutes were needed to fully charge each set of batteries.

Another issue encountered in the field was that the batteries did not start charging until they cooled down to a certain temperature. Especially after each flight and due to open sunny and hot weather conditions the batteries over-heated, and this made it difficult to continue the data collection process.

In addition to drone battery charging difficulties, maintaining sufficient battery power on mobile, iPad, and laptop devices was also a challenge.

3.1.4 UAV Attachments and Internet Connectivity

The DJI Matrice M600 was attached with MicaSense RedEdge multispectral and FLIR Duo Pro R thermal cameras to acquire high resolution imagery in this research. These two sensors were mounted on a custom designed gimbal on the drone. Both these sensors have delicate wiring connected from the drone control board and external battery supply. Protecting these wires during inspection and out in the field is challenging. However, with the latest drones, this problem can be eliminated with the use on onboard skyport gimbal adapter which controls the sensors within the drone manufacturing system.

To achieve successful data collection, all drones, sensors, and flight mission planning software must be connected to the internet in order to communicate with each other. Some of the settings on each sensor are adjusted using a mobile app before and after each flight. To connect these devices, a Verizon Jetpack hotspot (MiFi 8800L) device was used, however, since the research sites were in remote locations, maintaining a stable internet connection was challenging.

3.1.5 Post-flight and Safety

To ensure smooth flight operations, certain post-flight checklists and safety procedures are implemented following a successful landing of an aircraft. The procedure involves replacing of memory cards, cleaning of sensors, replacing batteries and recording flight logs.

Since this study involved high-frequency data collection process, several memory cards were used for storage of data captured from both sensors. After each flight, all the

data captured were copied to a laptop device and been fully formatted to have full storage capacity. This step was also crucial to verify that the data was being collected properly.

One common issue with conducting flights out in the field is ingress of small dust particles into the drones and sensors which can cause difficulties in data collections process. A high-pressure compressed can of air is used along with soft cloth and brush to clean the dust. During idle times, dust-sealed caps were used on sensors for safety.

After successful UAV mission, a flight log was used to record observations in the field at the time of flight. This included: start and end time of flight missions, date, location, temperature, relative humidity, wind speed, cloud cover and any remarks experienced during the flight.

3.2 Challenges of Multispectral and Thermal Imaging

3.2.1 Sensor Calibration

3.2.1.1 Calibration of MicaSense RedEdge Multispectral Camera

MicaSense RedEdge Multispectral Cameras were calibrated using an approach developed by Maguire, 2018. The procedure involves capturing two images of MicaSense calibrated panel reflectance (PR), before and after each flight, taken at waist level (Figure 3.1). Apart from reflectance panel images captured, a MicaSense Downwelling Light Sensor (DLS) is also mounted on the top of the drone to measures the irradiance for each individual image during the flight, and is stored in the image metadata. Using theses images as input, the Pix4D Mapper (Pix4D) software was used to calibrate and stitch the ortho-mosaics.

There are a number of factors that must be considered when obtaining calibrated multispectral images. That includes effects of sun angle, cloud coverage and canopy shadows. The best time to capture multispectral images is during solar noon, when solar irradiance values have less difference and clouds are minimal or absent. Since, this research aims to obtain imagery during multiple times in day, data sets with high cloud cover and canopy shadow imagery at late evening have been omitted.

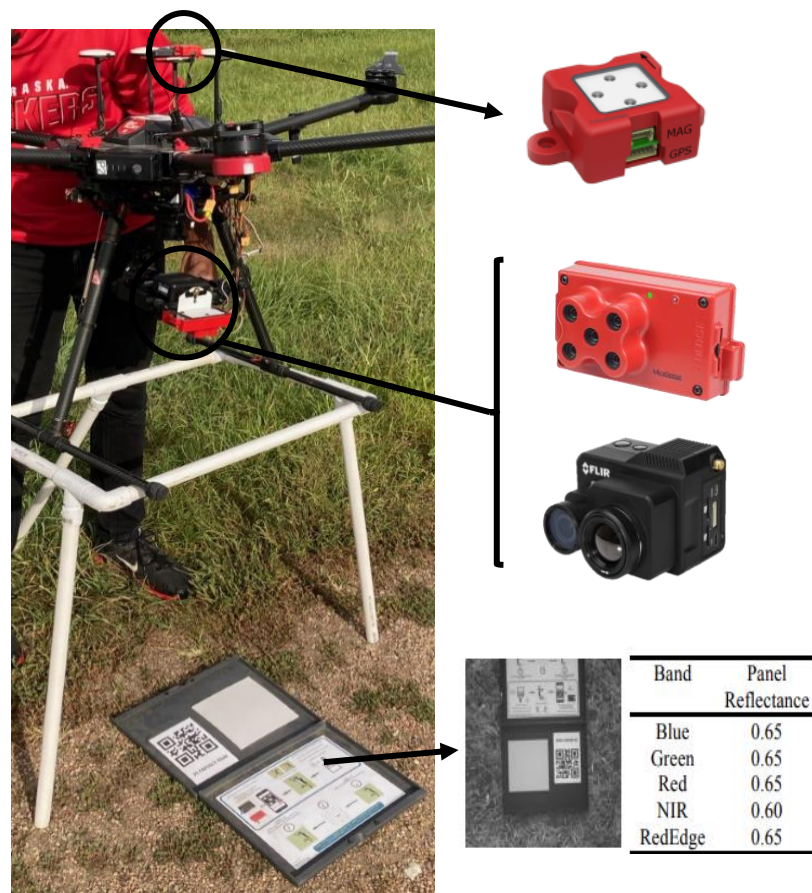| Band	Panel Reflectance
Blue	0.65
Green	0.65
Red	0.65
NIR	0.60
RedEdge	0.65

Figure 3. 1 Capturing of MicaSense RedEdge Panel Reflectance (PR) using a stand at waist level. Images on the left in sequence are – MicaSense Downwelling Light Sensor (DLS), MicaSense RedEdge Multispectral Camera, FLIR Duo Pro R 640 Thermal Camera and an image with PR reflectance values used in Pix4D multispectral calibration processing

3.2.1.2 Calibration of FLIR Duo Pro R Thermal Camera

The calibration of thermal images for FLIR Duo Pro R camera used in this research was developed by Maguire, (2021). The calibration process accounted for both atmospheric and radiometric corrections and remodified for this research at an altitude of 400ft (120 m AGL). The linear thermal calibration model procedure and methodology have been explained in chapter 2.

The major requirement involved in using the Thermal Calibration Model is the use of Infrared Thermometer (IRT) information at the time of the flight from the selected research sites. Among the three research sites, only ENREC1 IRT data was fully usable at all flight times, data taken from Singh et al. (2021). ENREC2 IRT data was limited due to different research objectives carried out by Bhatti et al., (2021), and only a few flight times were used in the model. SCAL site did not have any IRTs at the location. As a result, the overall model used for training model coefficients was mostly or exclusively based on ENREC1 IRT information and in comparison with Maguire, (2021), model, in which he used only ENREC1 IRT information to calibrate this thermal imagery.

The IRTs used for ENREC1 were all tested and calibrated before the start of the 2020 growing season with Singh et al. (2021) (Figure 3.2) for temperature accuracy and applied further to Planks equation to correct for emissivity using Maguire, (2021).

Another issue with the FLIR Duo Pro Thermal camera used in this study is to manually trigger Flat Foot Correction (FFT), commonly referred to as shutter calibration, every ten seconds during the time of flight. This is necessary for thermal cameras to re-calibrate the sensor array to account for changes in camera body temperature and pixel

drift (Maguire., 2021). On many occasions, the FCC was not triggered after exactly 10 seconds, which resulted in some missing images once the data was moved to storage.
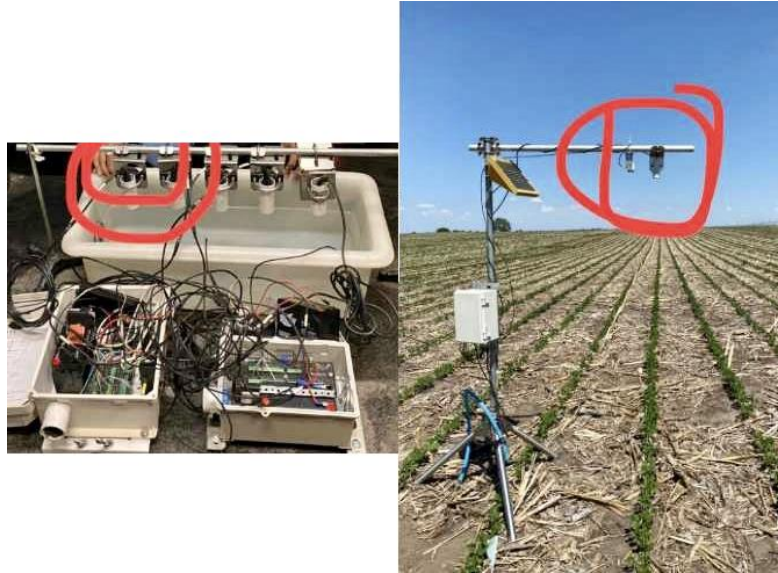
Figure 3. 2 Left: Conducting water bath experiment using Apogee Infrared Thermometer (IRTs) along with Data logger for calibration of IRT temperature values. Right: Sensor node station showing the IRT mounted at a 45 degree angle in ENREC1 during 2020 early growing season.

Finally, the thermal camera requires sensor warming up time, before it can be used for flight mission at the start of each day. Failure to follow any of the above steps will result in a poor thermal image dataset and inaccurate pixel temperature values. For maximum accuracy of the final imagery, all practices have been accounted for in this research.

3.2.2 Image Processing Issues

The very common issues that occur during image processing steps are – camera focus issues – Motion Blur, missing (EXIF) GPS information, missing images and overlap issues.

Camera focus issues are caused when the sensor cannot focus or lock on the required target, and this causes some blurry effects at certain parts of the imagery. This happens when the drone is operated at higher speed than the the time required for the image to be captured. Sometimes motion blur can also be caused due to strong wind gusts in between the flight times. Figure 3.3 is an example of motion blur captured while conducting flights at ENREC1.
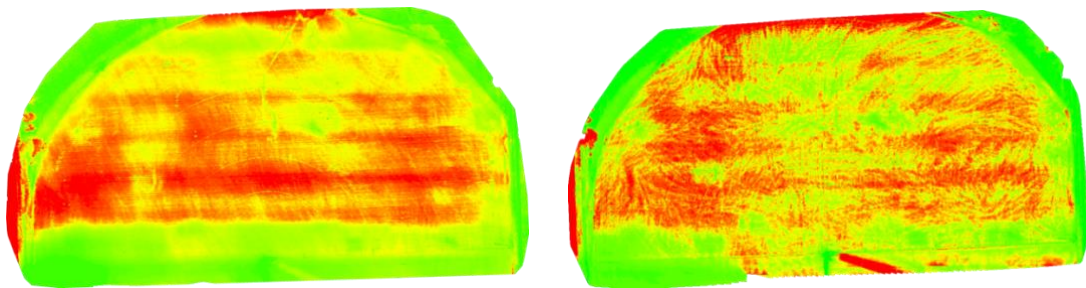
Figure 3. 3 Left: Example image from a thermal camera with motion blur, taken from ENREC1. Right: Example image from thermal camera affected by wind, taken from ENREC1

The next possible processing error results from missing (EXIF) data which is needed for an image to be geo-located. During the course of high-frequency UAV operations, some of the images captured did not store metadata or information about the location of the image. When processed with Pix4D software, images without metadata cause an error to appear that forces the images to be discarded or manually uploaded. Due to the fact that this research used two sensors at the same time, some of the images were restored from sensor to restore the other. Still, some images were discarded when neither sensor returned any information. An example of this error is shown in image 3.4.
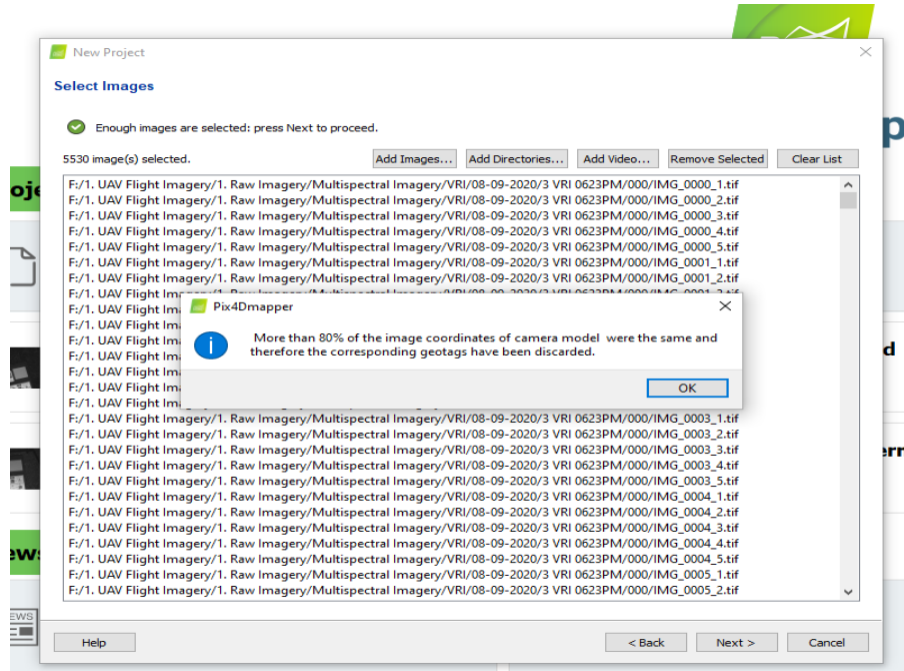
Figure 3. 4 Example error output from Pix4D Mapper indicating
that more than 80% of the images are not geolocated.

As discussed above, missing of some images during flights can cause errors

during image processing and considerable effects on final imagery. Possible reasons that

cause missing images are – improper triggering of FFC, missing EXIF data, wireless or

magnetic interference or system error due to overheating of sensors. These missing

images can cause gaps in the processed ortho-mosaic images retrieving no spectral or

reflectance information. Additionally, the front and side overlap percentage setting can

also create missing images and poor stitching while processing the datasets. The

resolution of sensor and flight altitude can also cause inaccuracies in the imagery. Below

Figure 3.5 shows an example of missing imagery of thermal dataset at ENREC2.
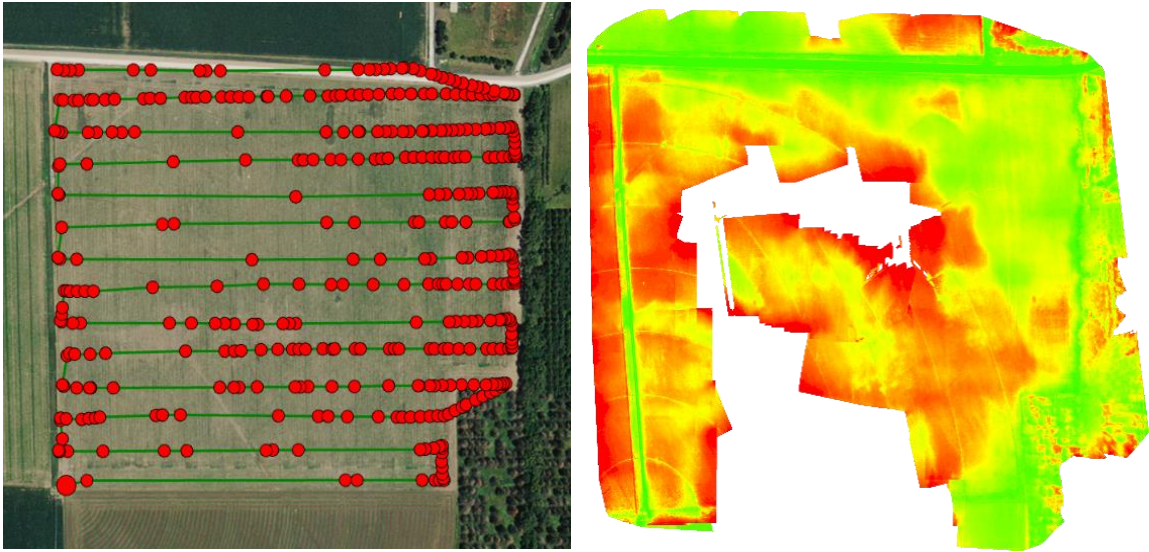
Figure 3. 5 Left: Example image of missing thermal images before generating output in Pix4D Mapper. Base Image: Google Earth Hybrid, 2020. Right: Processed thermal image showing gaps with uneven distribution of temperature values if neighboring images.

3.2.3 Data Storage

This research required enormous amounts of storage space during in-flight operations (SD Cards for both sensors) and post-flight operations (image processing outputs). Both raw and processed imagery are required to be stored in correct file destinations for easy access and re-processing options. More storage space is required when these processed imagery are being used for ArcGIS applications. All these imagery, along with flight logs, custom EXIF data, and other required meteorological data have been stored with multiple backup options, using portable hard drives and cloud storage for retrieving the data at all times.

Finally, this study was carried out with great care, taking into account of all of the factors that contribute to successful data collection and storage, with backups.

3.3 Water Stress Mapping

The overall objective of this research project is to develop water stress maps based on high-frequency UAV data captured from multispectral and thermal cameras to identify the temporal nature of crop stress pattern and recovery. The statistical based CWSI approach used in the research is quite new and only a few papers has been published using this approach (Park et al., 2017, 2018, 2021; Bian et al., 2019).

After an extensive data collection process, the steps and challenges involved in generating water stress maps include –

- Careful examination of orthomosaic images and eliminating datasets containing missing and unsuitable imagery.

- Downscaling and resampling of multispectral images to match thermal image resolution.

- Study and use of python packages (GDAL, rasterio, numpy, matplotlib, pandas, scipy, etc.) to develop T_{wet} and T_{dry} thresholds.

- Knowledge of Data Management and Spatial Analyst Tools on ArcMap for creating NDVI, NDRE, (ΔT), CWSI and DANS maps, and also for extraction of multi values for development of correlation plots between two selected variables.

- Troubleshooting on python and ArcGIS for potential problems and debugging.

To sum up, the evaluation of results in this study has compelled in understanding some new knowledge on understanding of the temporal and spatial crop stress patterns.

3.4 Deviations in Research

The original objective of this research project involves deployment of unmanned aircraft six times in a day for monitoring of crop response to one irrigation event till next successive irrigation event. However, due to the following factors addressed in this chapter – like weather, battery and charging time, internet connectivity, sensor issues, and post-image processing issues, tentative revisions were done to meet the original objectives as closely as possible. Another major factor that caused deviation in this research was the COVID-19 outbreak during 2020 growing season. The pandemic situation led to university lockdown and requirement to follow some protocols to continue the research. Thus, the data collection process at the start of growing season was delayed.

3.5 Conclusion

In conclusion, much effort has been put into this research and this chapter has addressed some of the challenges related to the data collection and post-processing stages. The issues mentioned in this chapter will help future researchers in improving their methods and show the extent and possibilities of using unmanned aerial vehicle (UAV) technology for high-frequency data collection.

3.6 References

Bhatti, S., D. M. Heeren, S. A. O'Shaughnessy, S. R. Evett, M. S. Maguire, S. P. Kashyap, and C. M. U. Neale. 2021. Comparison of stationary and mobile canopy sensing systems for irrigation management of maize and soybean in Nebraska. Applied Engineering in Agriculture (in review).

Bian, J., Zhang, Z., Chen, J., Chen, H., Cui, C., Li, X., ... & Fu, Q. (2019). Simplified

    evaluation of cotton water stress using high resolution unmanned aerial vehicle

    thermal imagery. Remote Sensing, 11(3), 267.

Maguire, M. S. (2018). An evaluation of unmanned aerial system multispectral and

    thermal infrared data as information for agricultural crop and irrigation

    management (Doctoral dissertation, University of Nebraska-Lincoln).

Maguire, M. S., Neale, C. M., & Woldt, W. E. (2021). Improving Accuracy of Unmanned

    Aerial System Thermal Infrared Remote Sensing for Use in Energy Balance

    Models in Agriculture Applications. Remote Sensing, 13(9), 1635.

NOAA Office of Satellite and Product Operations, (1994): NOAA Geostationary

    Operational Environmental Satellite (GOES) I-M and N-P Series Imager Data.

    [indicate subset used]. NOAA National Centers for Environmental Information.

    doi:10.25921/Z9JQ-K976. [access date] (https://www.goes.noaa.gov/).

Park, S. (2018). Estimating plant water stress and evapotranspiration using very-high-

    resolution (VHR) UAV imagery (Doctoral dissertation).

Park, S., Nolan, A., Ryu, D., Fuentes, S., Hernandez, E., Chung, H., & O'connell, M.

    (2015, November). Estimation of crop water stress in a nectarine orchard using

    high-resolution imagery from unmanned aerial vehicle (UAV). In Proceedings

    of the 21st International Congress on Modelling and Simulation, Gold Coast,

    Australia (Vol. 29).

Park, S., Ryu, D., Fuentes, S., Chung, H., Hernández-Montes, E., & O'Connell, M.

    (2017). Adaptive estimation of crop water stress in nectarine and peach orchards

using high-resolution imagery from an unmanned aerial vehicle (UAV). Remote

Sensing, 9(8), 828. https://www.mdpi.com/215938

Park, S., Ryu, D., Fuentes, S., Chung, H., Hernández-Montes, E., & O'Connell, M.

(2017). Adaptive estimation of crop water stress in nectarine and peach orchards

using high-resolution imagery from an unmanned aerial vehicle (UAV). Remote

Sensing, 9(8), 828.

Singh, J., Ge, Y., Heeren, D. M., Walter-Shea, E., Neale, C. M., Irmak, S., ... & Maguire,

M. S. (2021). Inter-relationships between water depletion and temperature

differential in row crop canopies in a sub-humid climate. Agricultural Water

Management, 256, 107061.

United States. National Weather Service. (1995). Welcome to the National Weather

Service. Silver Spring, MD :The Service (https://forecast.weather.gov/)

Appendix

Table: UAV Flight Log Database

Year	Date	Time	Location	Temp	RH	Wind	Altitude	Thermal Imagery	Multispectral Imagery
2020	8/8/2020	0846AM	ENREC2	24.14	88.68	3.71	120 m AGL	X	X
2020	8/8/2020	0955AM	ENREC1	24.96	85.88	4.38	120 m AGL	-	X
2020	8/8/2020	1056AM	ENREC2	26.14	81.65	4.72	120 m AGL	X	X
2020	8/8/2020	1144AM	ENREC1	27.22	78.1	4.58	120 m AGL	X	X
2020	8/9/2020	0941AM	ENREC2	26.04	72.38	3.06	120 m AGL	X	X
2020	8/9/2020	1052AM	ENREC1	27.73	64.02	4.39	120 m AGL	X	-
2020	8/9/2020	0242PM	ENREC2	30.1	66.57	4.12	120 m AGL	X	X
2020	8/9/2020	0419PM	ENREC1	31.08	63.62	3.39	120 m AGL	X	-
2020	8/9/2020	0519PM	ENREC2	31.19	65.5	2.86	120 m AGL	X	-
2020	8/9/2020	0623PM	ENREC1	30.64	69.65	2.75	120 m AGL	X	-
2020	8/9/2020	0724PM	ENREC2	29.45	76.28	1.69	120 m AGL	X	-
2020	8/9/2020	0844PM	ENREC1	27.32	82.67	1.46	120 m AGL	-	-
2020	8/10/2020	0247PM	ENREC1	27.75	49.82	2.02	120 m AGL	X	-
2020	8/10/2020	0401PM	ENREC2	27.99	52.78	2.35	120 m AGL	X	-
2020	8/10/2020	0519PM	ENREC1	27.77	54.22	2.61	120 m AGL	X	-
2020	8/10/2020	0605PM	ENREC2	27.04	56.21	2.92	120 m AGL	X	-
2020	8/10/2020	0700PM	ENREC1	24.92	64.95	2.96	120 m AGL	X	-
2020	8/10/2020	0747PM	ENREC2	22.23	76.33	1.38	120 m AGL	X	-
2020	8/11/2020	0941AM	ENREC2	22.05	69.46	3.31	120 m AGL	X	-
2020	8/11/2020	1038AM	ENREC1	24.38	67.97	3.39	120 m AGL	X	-
2020	8/11/2020	1134AM	ENREC2	26.25	66.43	3.18	120 m AGL	X	-
2020	8/11/2020	1235PM	ENREC1	27.62	64.81	2.82	120 m AGL	X	-
2020	8/11/2020	0156PM	ENREC2	28.7	64.03	2.8	120 m AGL	X	-
2020	8/25/2020	1015AM	ENREC2	28.19	57.94	3.17	120 m AGL	X	X
2020	8/25/2020	1110PM	ENREC1	30.06	51.42	3.87	120 m AGL	X	X

| 2020	8/26/2020	1037AM	ENREC2	29	52.61	3.83	120 m AGL	X	X
2020	8/26/2020	1125AM	ENREC1	31.18	44.25	5.12	120 m AGL	X	X
2020	8/26/2020	0130PM	ENREC2	33.51	36.12	5.13	120 m AGL	X	X
2020	8/26/2020	0220PM	ENREC1	33.84	34.55	5.16	120 m AGL	X	X
2020	8/26/2020	0345PM	ENREC2	33.83	34.01	5.09	120 m AGL	X	-
2020	8/26/2020	0432PM	ENREC1	33.84	30.17	5.03	120 m AGL	X	X
2020	8/26/2020	0604PM	ENREC2	31.73	38.05	3.09	120 m AGL	X	X
2020	8/26/2020	0654PM	ENREC1	28.59	51.54	1.8	120 m AGL	X	X
2020	8/28/2020	1057AM	SCAL	25.65	82.03	2.71	120 m AGL	X	X
2020	8/28/2020	0134PM	SCAL	28.9	67.94	3.04	120 m AGL	X	-
2020	8/28/2020	0410PM	SCAL	31.05	58.85	3.37	120 m AGL	X	X
2020	8/31/2020	1152AM	SCAL	25.58	56.7	1.6	120 m AGL	X	X
2020	8/31/2020	0138PM	SCAL	28.02	46.37	1.93	120 m AGL	X	X
2020	8/29/2020	1003AM	ENREC1	20.67	80.71	3	120 m AGL	X	-
2021	8/29/2020	1123AM	ENREC2	19.33	84.75	2.34	120 m AGL	X	-
2020	9/1/2020	0130PM	SCAL	23.42	77.84	1.8	120 m AGL	X	X
2020	9/1/2020	0337PM	SCAL	26.58	61.91	2.41	120 m AGL	X	X
2020	9/1/2020	0532PM	SCAL	26.44	59.82	2.7	120 m AGL	X	X
2020	9/3/2020	1246PM	SCAL	27.71	52.59	3.96	120 m AGL	-	-
2020	9/3/2020	0300PM	SCAL	30.04	50.17	3.66	120 m AGL	-	X
2020	9/3/2020	0548PM	SCAL	29.81	53.94	3.55	120 m AGL	-	-
2020	9/4/2020	1246PM	SCAL	29.03	52.76	3.07	120 m AGL	-	-

Figures
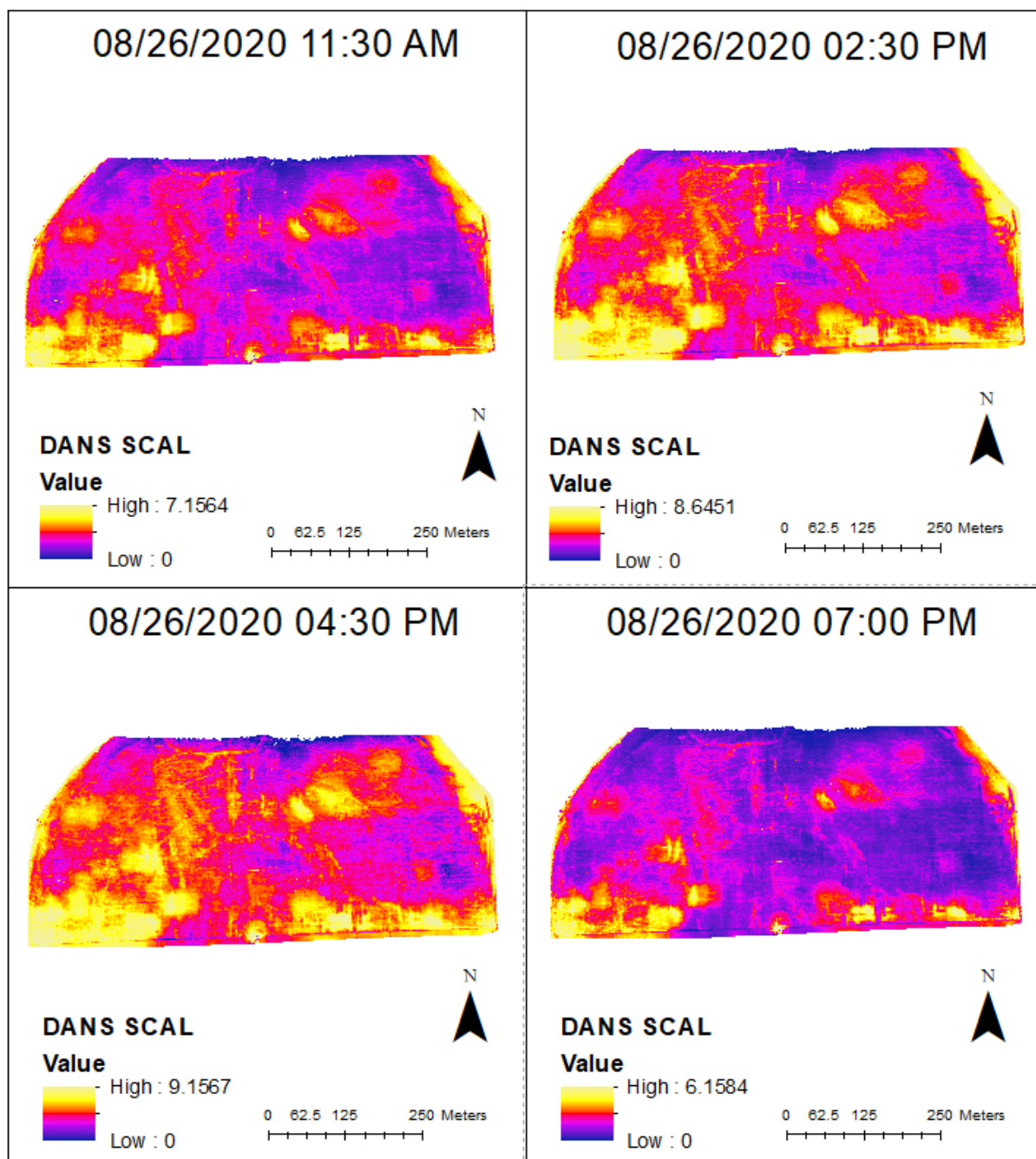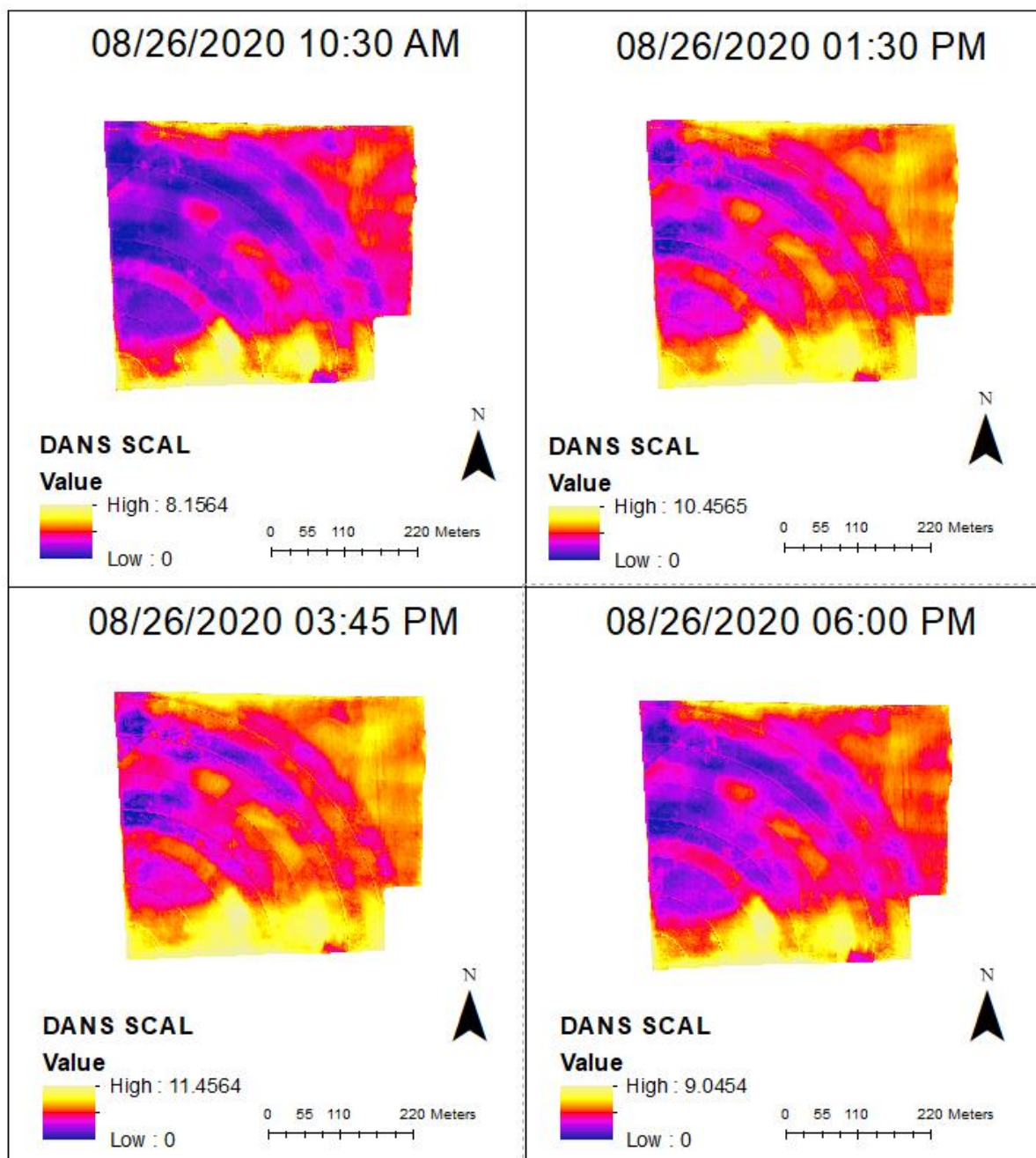
ENREC1 CWSI Maps
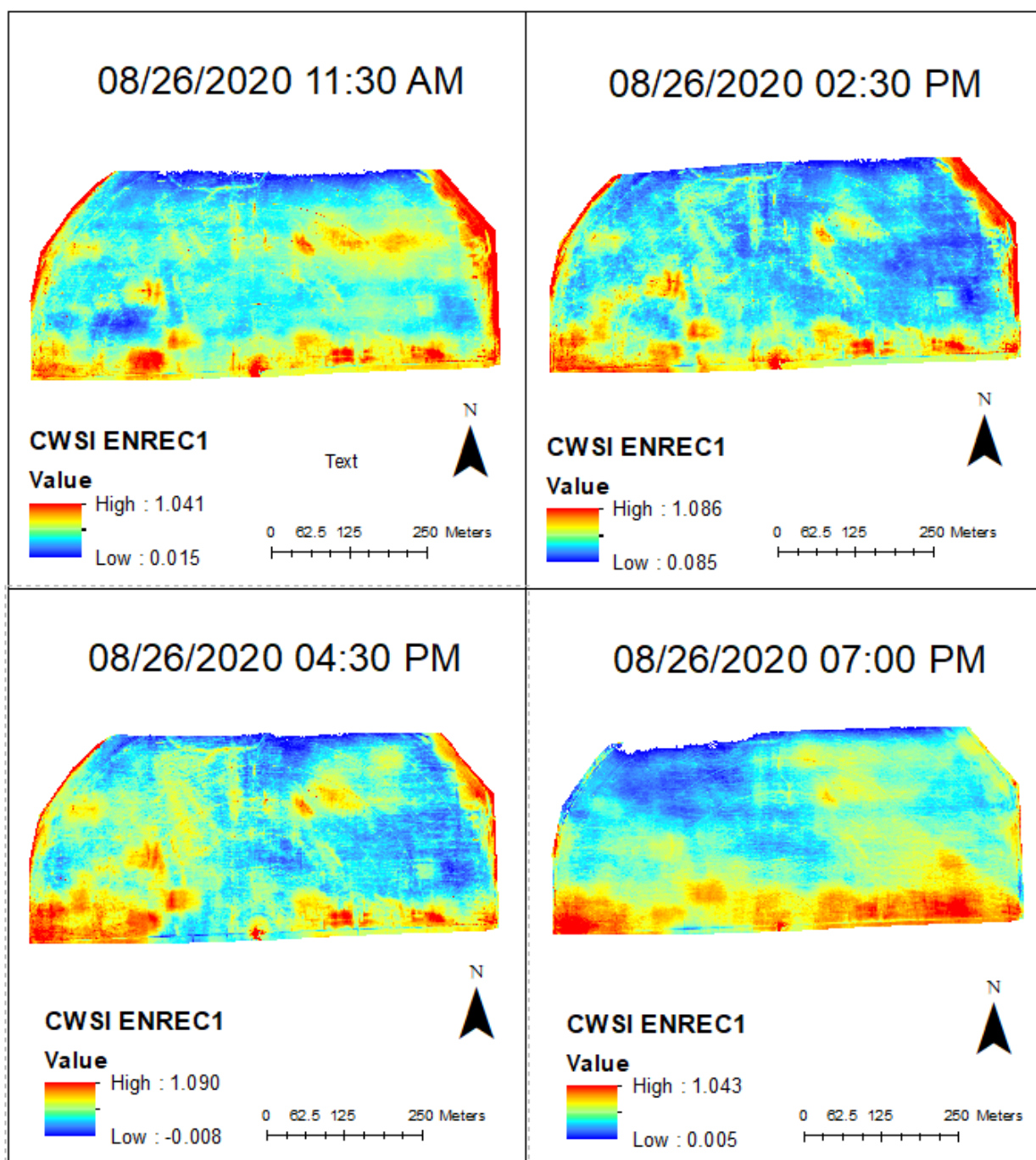
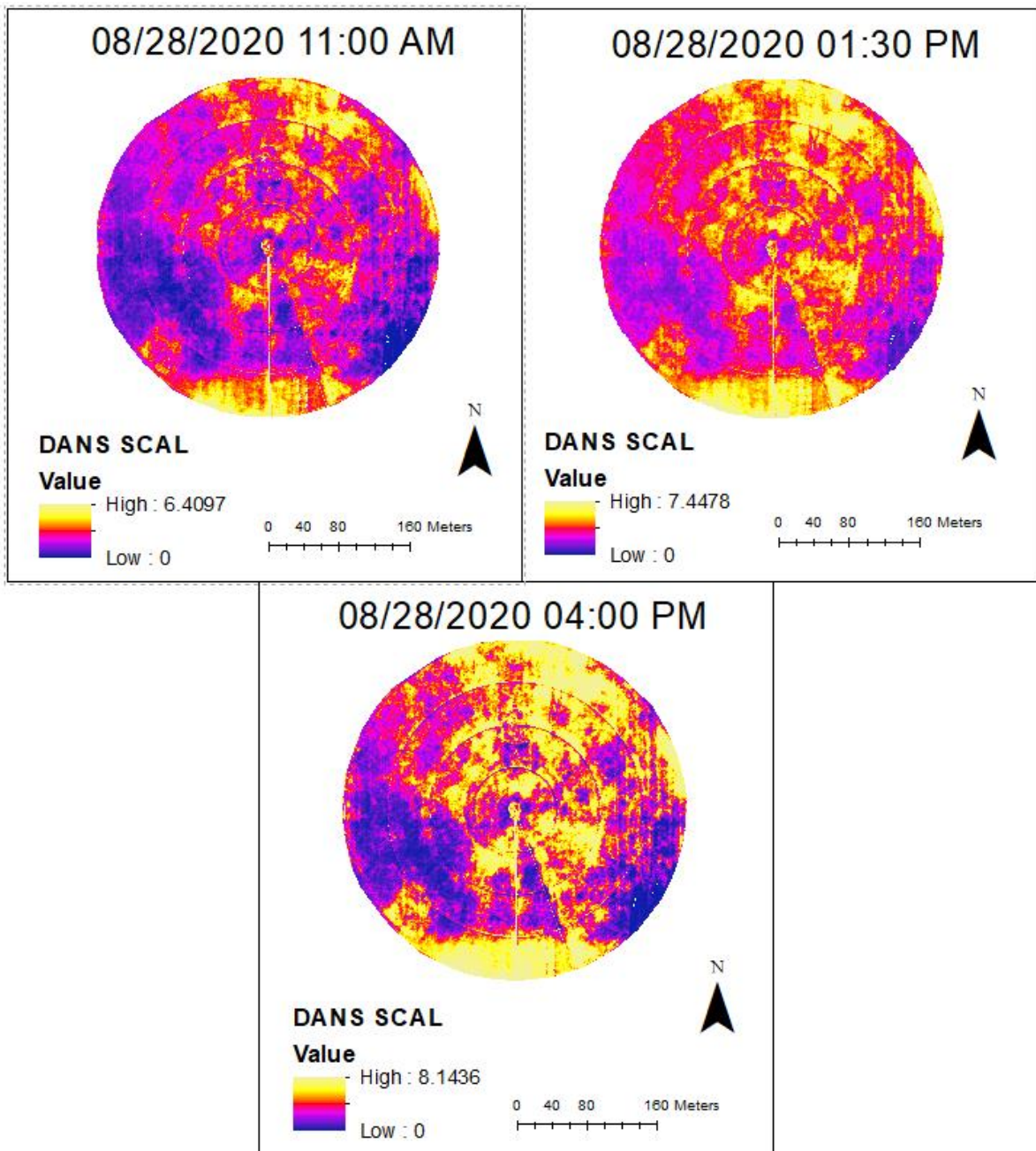ENREC2 CWSI Maps
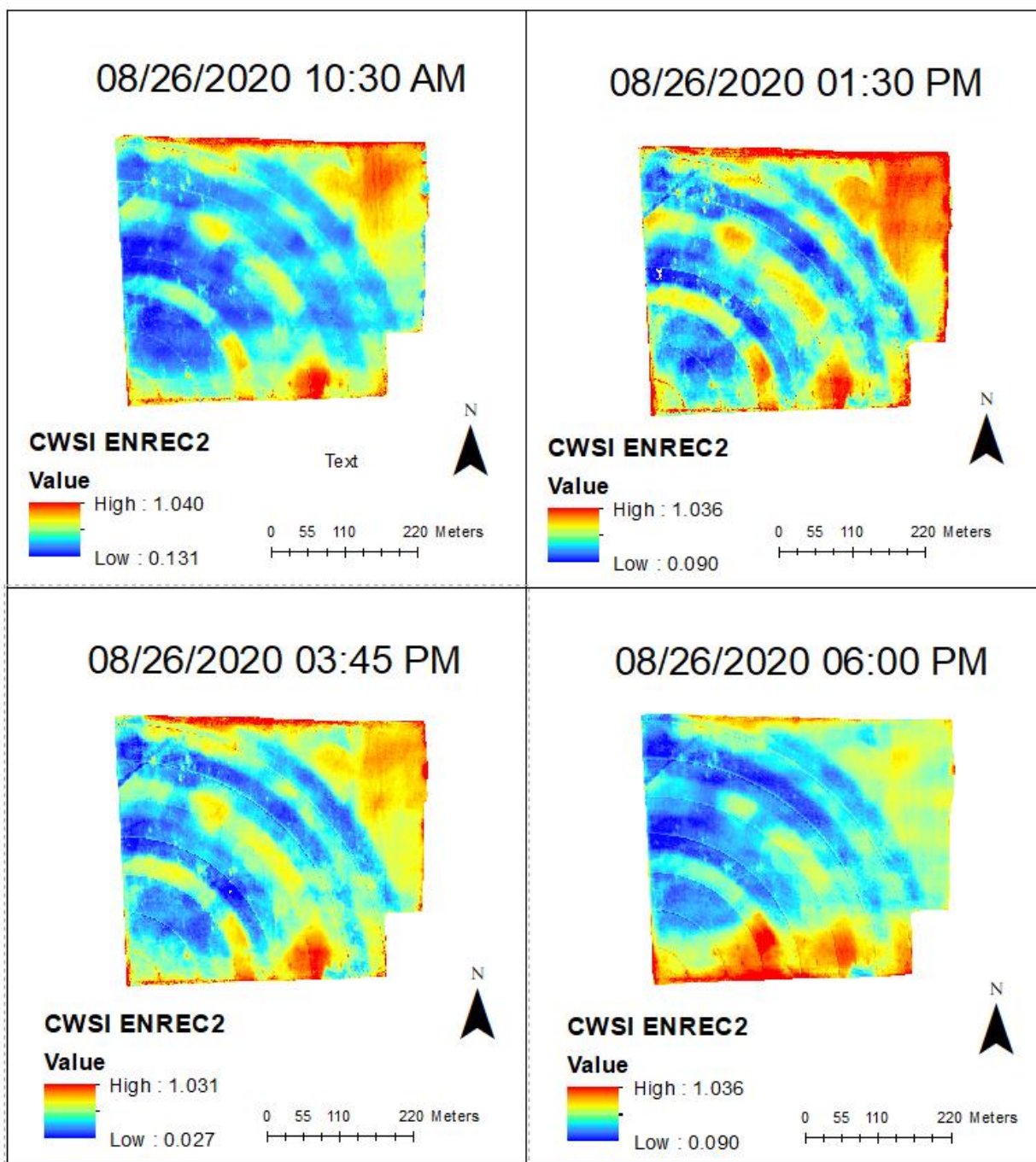
SCAL CWSI Maps
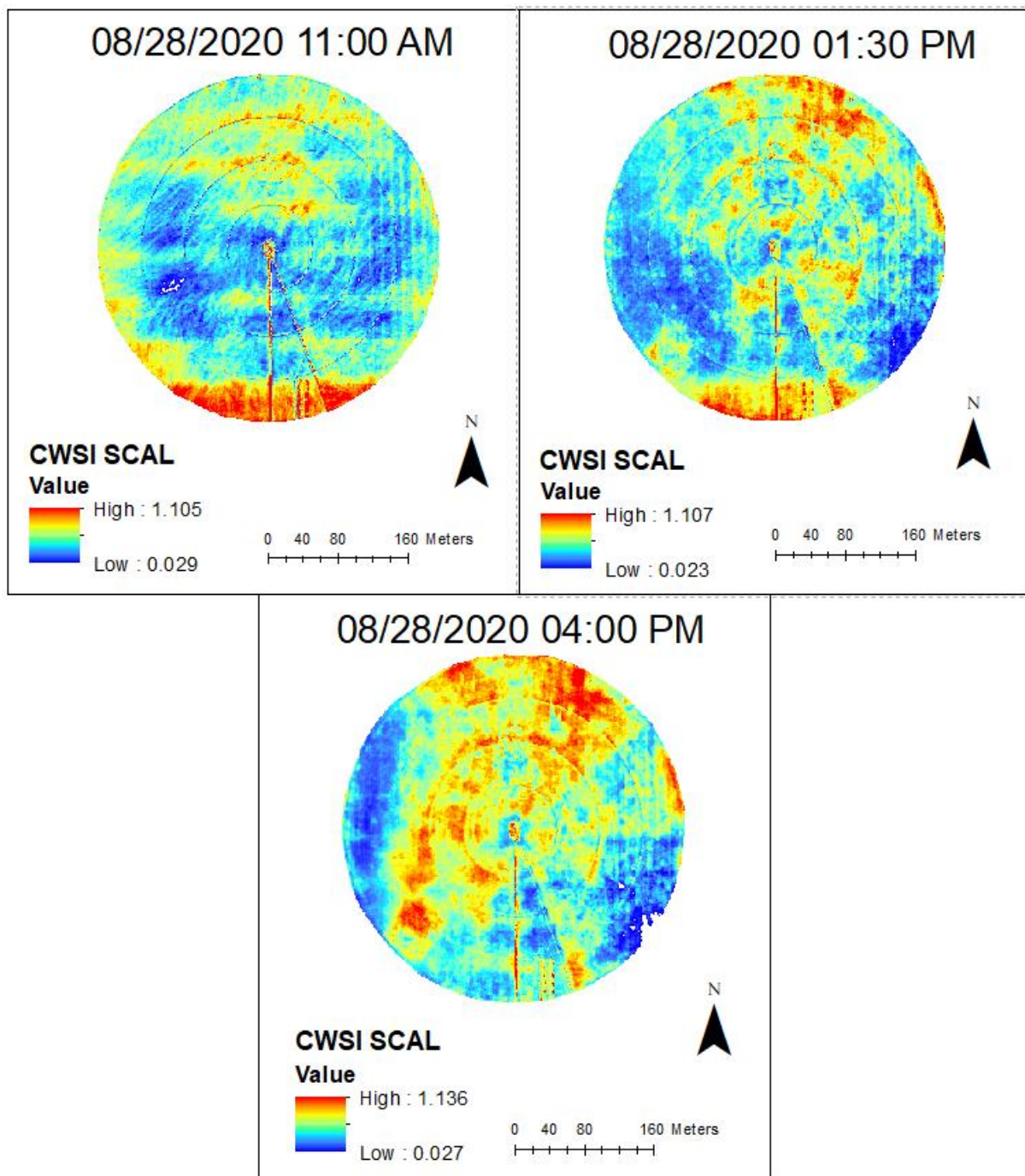
ENREC1 DANS Maps

ENREC2 DANS Maps

SCAL DANS Maps

Code: Extraction of T_{wet} and T_{dry} Values

```python
#Add all libraries
import rasterio
from rasterio.plot import show
import numpy as np
import pandas as pd
from matplotlib import pyplot as plt
import seaborn as sns
import os
import matplotlib.pyplot as plt
import rioxarray as rxr
import earthpy as et
import cv2 as cv
from skimage import feature
import scipy.stats as st
from osgeo import gdal
from sklearn.mixture import GaussianMixture as GMM

# Insert Tiff image froma folder
fp = r"image path "
img = rasterio.open(fp)
show(img)

# Open data
fps = rxr.open_rasterio(fp, masked=True)
plt.show()

# For Maximum and Minimum Values
print('Min:', np.nanmin(fps))
print('Max:', np.nanmax(fps))

#convert nan values to numbers
if np.all(fps):
    value = np.nan_to_num(fps)
value

#fit within the boundary of the image and open (resets the extent)
with rasterio.open(fp) as src:
   oviews = src.overviews(1)
   oview = oviews[-1]
   print('Decimation factor= {}'.format(oview))
   thumbnail = src.read(1, out_shape=(1, int(src.height // oview), int(
src.width // oview)))

print('array type: ',type(thumbnail))
print(thumbnail)

plt.imshow(thumbnail)
```

```python
#convert any nan value again to 0 (zero)
thumbnail = thumbnail.astype('f4')
thumbnail[thumbnail==0] = np.nan

#add matrix to different variable name
data = thumbnail

#convert matrix to an array
val = np.array(data)

#remove values less than zero in the array
val[val<0]=0

#Custom variable for Gaussian Mixture Model
X = val

#Train GMM syntax for bimodal distribution
gm = GMM(n_components=2, max_iter=1000, covariance_type='full').fit(X)

#check GMM recreated GMM
print(gm.means_) #Need Further steps to extract and then follow below

#recreating new values and removing zeros
reval = val[val !=0]

#Check array
reval

#plot the new image
plt.imshow(val)

#requires mean and sigma for conifendense interval
mean, sigma = np.mean(reval), np.std(reval)

mean

sigma

#Extracting Twet and Tdry from Confidence Interval Syntax
from scipy import stats
conf_int = stats.norm.interval(0.99, loc=mean, scale=sigma)

#Shows Twet and Tdry values (lower and upper CIs)
conf_int
```